UNIVERSITAT DE BARCELONA

Impact of ultrasoft neutrinos and realistic radial wavefunctions on neutrinoless double-beta decay matrix elements

Master's degree in Nuclear Physics
Master's thesis

by
Pablo Soriano Fajardo

Advisor:
Dr. Javier Menéndez Sánchez (UB, Barcelona)

University of Seville (US)
University of Barcelona (UB)
November 2020

Contents

1 Introduction

Precise calculations of the neutrinoless double-beta $0\nu\beta\beta$ decay nuclear matrix elements (NME) used to calculate the $0\nu\beta\beta$ decay rate are relevant to the study of neutrino physics, since this decay rate also depends on a combination of the neutrino masses and mixing matrix elements. Our goal will be to improve the calculations of these NME by including previously neglected precision components, such as the contribution of very low-momentum (ultrasoft) neutrinos (Chapter 2) and the use of realistic radial wavefunctions (Chapter 3).

In this starting chapter, we will introduce and discuss the basic concepts that will make up the foundations of this work, as well as its objectives. In the first section (1.1) we will deal with the concept of neutrinoless double-beta decay and its significance and interest towards neutrino physics. In the second section (1.2), we will provide an insight of the nuclear shell model, which will be the framework of our calculations.

1.1 Neutrinoless double-beta decay and neutrino physics

Double-beta decay is a transition between isobaric nuclei in which two neutrons simultaneously decay into protons, meaning that the parent nucleus decays into a daughter nucleus with two fewer neutrons and two more protons. Being a second-order weak-interaction process, it is strongly suppressed and only observable for isotopes in which single beta decay is forbidden. This results in typical half-lives ranging from 10^{18} to 10^{24} yr, as observed in 11 different nuclei undergoing $\beta\beta$ decay [1] and 3 undergoing double electron capture $\varepsilon\varepsilon$ [2]. So far, all measured double-beta decay processes have been two-neutrino double-beta ($2\nu\beta\beta$) decay (corresponding to Figure 1a), which can be expressed as

$$ {}^{\mathrm{A}}_{\mathrm{Z}}\mathrm{X} \longrightarrow {}^{\mathrm{A}}_{\mathrm{Z+2}}\mathrm{Y} + \mathrm{e}^-_1 + \mathrm{e}^-_2 + \bar{\nu}_{e,1} + \bar{\nu}_{e,2}\,, \tag{1} $$

where ${}^{\mathrm{A}}_{\mathrm{Z}}\mathrm{X}$ and ${}^{\mathrm{A}}_{\mathrm{Z+2}}\mathrm{Y}$ are the parent and daughter nuclei; A,Z and N are the number of nucleons, protons and neutrons (such that $N = A - Z$), $e^-_{1,2}$ are the emitted electrons and $\bar{\nu}_{e;1,2}$ are the emitted antineutrinos.

One particular detail about neutrinos is that they are the only neutral fermions we know of. As such, neutrinos are the only known particles that may be Majorana fermions, which means that they would be their own antiparticle. This would imply the existence of a yet-hypothetical alternate decay mode, the neutrinoless double-beta ($0\nu\beta\beta$) decay

$$ {}^{\mathrm{A}}_{\mathrm{Z}}\mathrm{X} \longrightarrow {}^{\mathrm{A}}_{\mathrm{Z+2}}\mathrm{Y} + \mathrm{e}^-_1 + \mathrm{e}^-_2 \tag{2} $$

As their own antiparticle, Majorana neutrinos could virtually annihilate each other in the decay, as depicted in Figure 1b.

The inverse half-life of a $0\nu\beta\beta$ decay between $J^P = 0^+$ states of the parent and daughter nuclei can be written as

$$ \left[T^{0\nu}_{1/2}\,(0^+_i \to 0^+_f)\right]^{-1} = G_{0\nu}(Q_{\beta\beta}, Z)\, g_A^4\, |M^{0\nu}|^2\, m^2_{\beta\beta}\,, \tag{3} $$

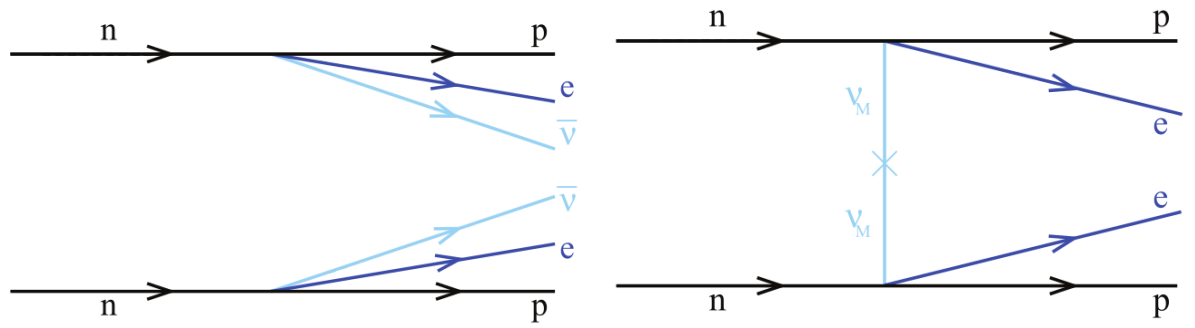

(a) Two-neutrino double-beta decay (b) Neutrinoless double-beta decay

Figure 1: Feynman diagrams for (a) $2\nu\beta\beta$ and (b) $0\nu\beta\beta$ decay. Two neutrons (n) decay into two protons (p), emitting two electrons (e) and (a) two antineutrinos ($\bar{\nu}$) or (b) no neutrinos, implying that they are Majorana particles (ν_M) in the second case. From [3].

where $G_{0\nu}(Q_{\beta\beta}, Z)$ is a phase space factor that can be calculated with great precision [4],

$$Q_{\beta\beta} = E_i - E_f - 2m_e \tag{4}$$

is the Q value of the reaction, $M^{0\nu}$ is the "nuclear matrix element" (NME)

$$M^{0\nu} = M^{0\nu}_{GT} - \frac{g_V^2}{g_A^2} M^{0\nu}_F + M^{0\nu}_T, \tag{5}$$

with each of the terms corresponding to the Gamow-Teller, Fermi and tensor NME contributions, respectively. $g_V = 1$ and $g_A \simeq 1.27$ are the vector and axial coupling, and $m_{\beta\beta}$ a combination of the neutrino masses m_j and mixing matrix elements U_{ej}, defined as

$$m_{\beta\beta} \equiv \left| \sum_j m_j U_{ej}^2 \right| = \left| m_1 |U_{e1}|^2 + m_2 |U_{e2}|^2 e^{i(\alpha_2 - \alpha_1)} + m_3 |U_{e3}|^2 e^{i(-\alpha_1 - 2\delta)} \right|. \tag{6}$$

where m_j are the neutrino mass eigenstates (not the same as the neutrino flavor eigenstates: m_1 leaning heavily towards electron flavor, m_2 being a more even blend of the three lepton flavors and m_3 mostly muon and tau flavor), δ is the so-called Dirac phase and $\alpha_{1,2}$ are Majorana phases that vanish if neutrinos are Dirac particles [3].

Likewise, we can express the inverse half-life for $2\nu\beta\beta$ decay as

$$\left[T^{2\nu}_{1/2}\right]^{-1} = G_{2\nu}(Q_{\beta\beta}, Z)\, g_A^4 \left| M^{2\nu}_{GT} - \frac{g_V^2}{g_A^2} M^{2\nu}_F \right|^2 \simeq G_{2\nu}(Q_{\beta\beta}, Z)\, g_A^4 \left| M^{2\nu}_{GT} \right|^2. \tag{7}$$

where the Fermi contribution can be safely neglected when the isospin T of the initial and final nuclei is different.

Obtaining reliable values of $M^{0\nu}$ is key to obtain the value of $m_{\beta\beta}$, since experimentally observing a $0\nu\beta\beta$ decay would provide its half-life, $T^{0\nu}_{1/2}$. This would provide vital information about the absolute scale of the neutrino masses and, potentially, about its ordering. As illustrated in Figure 2, knowing the value of $m_{\beta\beta}$ along with the mass of the lightest neutrino (a parameter β decay experiments and cosmological observations like the KATRIN [5] and Planck [6] collaborations are sensible to) could confirm which of the neutrino-mass hierarchies is correct: the normal hierarchy ($m_1 < m_2 < m_3$) or the inverted hierarchy ($m_3 < m_1 < m_2$). This would have fundamental implications for neutrino physics and cosmology [7], since it could shed some light on the mechanism of neutrino mass generation.

$0\nu\beta\beta$ decay would violate the conservation of the total lepton number, as well as the conservation of the "$B-L$" quantity (baryon-lepton number), the latter being a fundamental symmetry of the Standard Model [1]. Accordingly, the detection of this process would imply Physics beyond the Standard Model. Additionally, the existence of the aforementioned violation of the lepton number could be very useful to explain the generation of the matter-antimatter asymmetry in our universe via a process known as "leptogenesis" [8, 9].

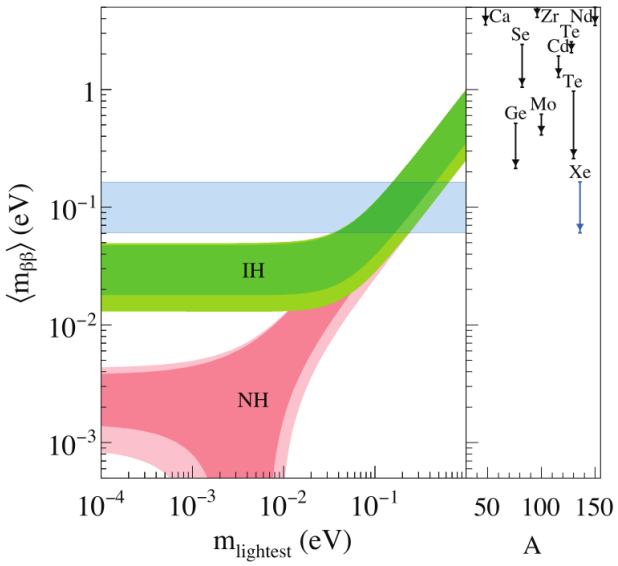

Figure 2: Left panel: bands for the value of the parameter $m_{\beta\beta}$ as a function of the mass of the lightest neutrino, for the case of normal (NH, red band) and inverted (IH, green band) neutrino-mass hierarchies. The present best experimental upper limits on $m_{\beta\beta}$ are shown in the blue band. Right panel: present best upper limits, with uncertainty bars, on $m_{\beta\beta}$ from experiments performed on each $\beta\beta$ emitter, as a function of mass number A. The uncertainty bands and bars include experimental uncertainties and ranges of calculated nuclear matrix elements. From [10].

1.2 The nuclear shell model

1.2.1 From the independent particle model to the interacting shell model

The nuclear shell model was originally introduced by M. Goeppert-Mayer [11] and H. Jensen et al. [12] to explain the regularities of the nuclear properties associated with magic numbers. They proposed an independent particle model, assuming that the main effect of the two-body nucleon-nucleon (NN) and three-body (3N) interactions was to generate a mean field [13].

This nuclear mean field was constructed as a surface corrected harmonic oscillator whose main novelty was the very strong spin-orbit splitting needed to explain these magic numbers [14]. It is described as follows:

$$U(r) = \frac{1}{2}m\omega^2 r^2 + D\boldsymbol{l}^2 - C\boldsymbol{l}\cdot\boldsymbol{s}, \tag{8}$$

where m is the mass of the particle, ω its the angular frequency, r its radial component, l and s are the angular momentum and spin operators (respectively) and C and D are parameters to be fit for best results.

Figure 3 shows the single particle levels of the nuclear mean field. From left to right, we first find the shell structure of the harmonic oscillator, then the splitting due to the $\boldsymbol{l}^2$ term in Equation (7) and, in the middle of the figure, the actual single particle levels, that take into account the spin-orbit splitting [14]. On the right hand side we find three rows of numbers corresponding to, respectively, the maximum occupancy of the level, the accumulated occupancy and the predicted magic numbers for protons and neutrons (2, 8, 20, 28, 50, 82 and 126). Alternately to the notation in Figure 3, the principal quantum number n of the lowest level is sometimes defined as $n = 0$ instead of $n = 1$, such that $N = 2n + l$. This is the convention we will be following.

The success of the independent particle model strongly suggests that the very singular free NN interaction can be regularized in the nuclear medium. Starting with this bare interaction, the exact solution of the many-body problem in the infinite Hilbert space built on the mean field orbits is approximated in the large scale shell model calculations by the solution of the Schrödinger equation in the valence space, using an effective interaction [13, 14] such that observables are preserved:

$$H|\Psi\rangle = E|\Psi\rangle \;\rightarrow\; H_{\text{eff}}|\Psi_{\text{eff}}\rangle = E|\Psi_{\text{eff}}\rangle. \tag{9}$$

Note that H_{eff} includes interactions between nucleons, therefore describing physics beyond the mean field of Equation (8).

In general, effective operators have to be introduced to account for the restrictions of the Hilbert space, such as

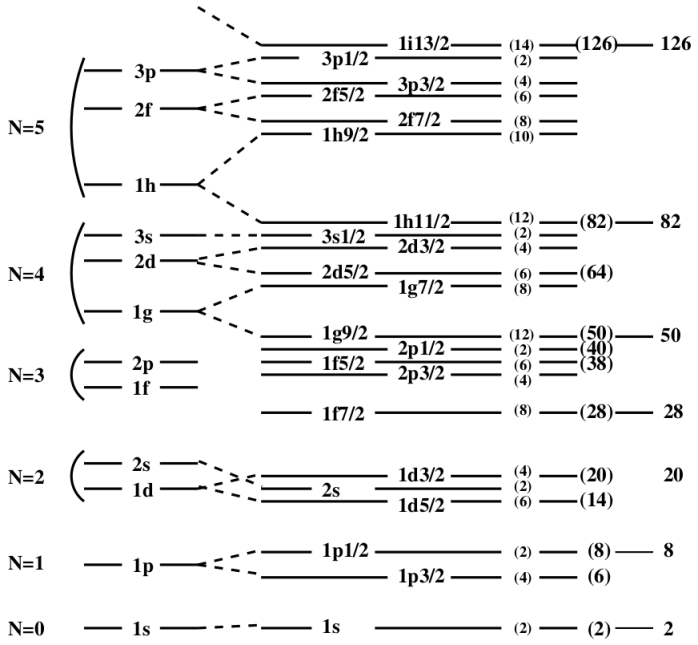

Figure 3: Structure of the spherical mean field, see text for details. From [14].

$$\langle \Psi | \mathcal{O} | \Psi \rangle = \langle \Psi_{\text{eff}} | \mathcal{O}_{\text{eff}} | \Psi_{\text{eff}} \rangle. \tag{10}$$

Once we adopt a regularized interaction that is compatible with the experimental mean field (in this case, magic numbers) we can proceed using the spherical mean field orbits as the basis for the occupation number space (Fock space). We will have states $i, j, k, ...$ with energies $\epsilon_i, \epsilon_j, \epsilon_k, ...$ that will bunch in shells, giving rise to magic numbers when the energy difference between them is large enough.

This motivates the separation of the full space intro three different regions:

- Inert core: encompasses the orbits that are always full, therefore not undergoing any change. If this core is made up of Z_c protons and N_c neutrons, there will remain $z_v = Z - Z_c$ valence protons and $z_v = N - N_c$ valence neutrons.
- Valence space: formed by the orbits that are available to the aforementioned valence particles, which will partially occupy them according to the dictates of the effective interaction H_{eff}.
- External space: refers to all the remaining orbits, which always remain empty.

In the valence space, a formal solution to the A-body problem can be obtained through the following procedure:

- First, we choose a single particle basis: $a_i^+|0\rangle$.

- We will then proceed to build the A-particle wavefunctions as Slater determinants:

$$|\Phi_\alpha\rangle = \prod_i^A a_i^+|0\rangle. \tag{11}$$

- The physical states are then expressed as a linear combination of these Slater determinants:

$$|\Psi_{\text{eff}}\rangle = \sum_\alpha C_\alpha|\Phi_\alpha\rangle. \tag{12}$$

- Lastly, the solution of the many-body problem $H_{\text{eff}}|\Psi_{\text{eff}}\rangle = E|\Psi_{\text{eff}}\rangle$ is given by the eigenvalues and eigenvectors of the many-body matrix $\langle\Phi_\alpha|H_{\text{eff}}|\Phi'_\alpha\rangle$.

1.2.2 The Lanczos method

If one aims to carry out large scale shell model calculations, standard diagonalization methods where CPU times increase as N_{dim}^3 [15, 16] (N_{dim} being the dimension of the many-body matrix) are not suitable. Taking into account that, in general, only a small number of eigenvalues and eigenvectors are needed, we can try to use another approach to this problem. This is where the Lanczos algorithm comes in handy.

The Lanczos method is based in the building of an orthogonal basis in which the many-body matrix has a tridiagonal structure. We initialize the algorithm with a normalized vector Φ_1 (that we call the "pivot" state) and apply the effective hamiltonian H_{eff} operator. We will then get a parallel and an orthogonal component of the pivot Φ_1:

$$H_{\text{eff}}|\Phi_1\rangle = E_{11}|\Phi_1\rangle + E_{12}|\Phi_2\rangle, \tag{13}$$

where $E_{11} = \langle\Phi_1|H_{\text{eff}}|\Phi_1\rangle$ and $E_{12}|\Phi_2\rangle = H_{\text{eff}}|\Phi_1\rangle - E_{11}|\Phi_1\rangle$.

Applying H_{eff} on Φ_2, we will generate a third vector Φ_3 orthogonal to Φ_1 and Φ_2:

$$H_{\text{eff}}|\Phi_2\rangle = E_{21}|\Phi_1\rangle + E_{22}|\Phi_2\rangle + E_{23}|\Phi_3\rangle, \tag{14}$$

where the hermicity of H_{eff} implies $E_{21} = E_{12}$. Analogously to the previous step, $E_{22} = \langle\Phi_2|H_{\text{eff}}|\Phi_2\rangle$, and E_{23} is obtained through normalization:

$$E_{23}|\Phi_3\rangle = (H_{\text{eff}} - E_{22})|\Phi_2\rangle - E_{21}|\Phi_1\rangle. \tag{15}$$

Continuing this process, at iteration n, we obtain the diagonal energy of the vector $|\Phi_n\rangle$, a new vector $|\Phi_{n+1}\rangle$ and the non-diagonal energy $E_{n,n+1}$:

$$E_{nn} = \langle\Phi_n|H_{\text{eff}}|\Phi_n\rangle, \tag{16}$$

$$H_{\text{eff}}|\Phi_n\rangle = E_{n,n-1}|\Phi_{n-1}\rangle + E_{nn}|\Phi_n\rangle + E_{n,n+1}|\Phi_{n+1}\rangle, \tag{17}$$

$$E_{n,n+1}|\Phi_{n+1}\rangle = (H_{\text{eff}} - E_{nn})|\Phi_n\rangle - E_{n,n-1}|\Phi_{n-1}\rangle, \tag{18}$$

always remembering that $E_{n,n-1} = E_{n-1,n}$. Due to H_{eff} being hermitic, the construction of the Lanczos matrix ensures that $E_{ij} = 0$ if $|i - j| > 1$, thus obtaining a tridiagonal matrix:

$$\begin{pmatrix} E_{11} & E_{12} & 0 & 0 & \cdots \\ E_{21} & E_{22} & E_{23} & 0 & \cdots \\ 0 & E_{32} & E_{33} & E_{34} & \cdots \\ 0 & 0 & E_{43} & E_{44} & \cdots \\ \vdots & \vdots & \vdots & \vdots & \ddots \end{pmatrix} \tag{19}$$

This matrix is diagonalized every certain number of steps. When the eigenvalues obtained through the diagonalization meet an established convergence criterion, the calculation will stop.

1.2.3 The choice of the basis

For a given valence space, the choice of the basis is simply driven by convenience. Depending on the properties we want to describe, one or another basis may be more appropriate. There are two possible choices: the m-scheme and the J-coupled scheme.

In the m-scheme, the basis is composed of all the Slater determinants made from all the possible partitions of the valence particles among every valence orbit $|nljm\tau\rangle$ [14], such that

$$|\Phi_\alpha\rangle = \prod_{i=nljm\tau} a_i^+|0\rangle. \tag{20}$$

where n, l, j, m and τ are the principal, orbital, total angular momentum, magnetic and isospin quantum numbers, respectively.

The principal advantage of this representation is the simplicity of the calculation of the many particle matrix elements, since they reduce to the two-body matrix elements of H in m-scheme with a phase [16]. Its major drawback, however, lies in the fact that only J_z and T_z are good quantum numbers, meaning that the basis takes into account all possible (J,T) states. This causes the dimensions of the matrix to be maximal, being proportional to

$$N_{\text{dim}} \propto \binom{d_\pi}{z_v} \cdot \binom{d_\nu}{n_v}, \tag{21}$$

where d_π and d_ν are the total degeneracies of the proton and neutron valence spaces and z_v and n_v are the valence protons and neutrons (as explained on section 1.2.1).

This is the basis the shell model code ANTOINE [15, 17] is based on, which we will use when we have to calculate states with $J \neq 0$ (for example, intermediate 1^+ states in a double-beta decay).

If one wants to avoid carrying on the full dimension of the m-scheme, one option is to implement "a priori" symmetries of the hamiltonian in the construction of the many particle basis. The full matrix is then divided in blocks and, for each ensemble of values with given quantum numbers, the dimensions are smaller. This is what we call the J-coupled scheme, and the dimensional reduction it provides turns out to be specially useful for $J = 0$, which is why we will be using the shell model code NATHAN [15] when we only have to deal with this kind of states.

However, when compared to the simplicity of the m-scheme, the calculation of the many-particle matrix elements is way more complex, involving products of cfp's (used to guarantee anti-symmetry) and $9j$ coefficients (related to angular momentum coupling).

2 Contribution of ultrasoft neutrinos to $0\nu\beta\beta$ decay

In this chapter, we follow an article by V. Cirigliano et al. [9] and introduce the ultrasoft contribution to the $0\nu\beta\beta$ decay amplitude: that is, the contribution of very low-momentum neutrinos to the total decay amplitude. In addition, we quantify for the first time the magnitude of this correction.

Our objective will be to calculate this new contribution ($M^{0\nu}_{\text{usoft}}$) for nuclei that have been experimentally observed to undergo double-beta decay (like ^{48}Ca $\rightarrow$ ^{48}Ti and ^{136}Xe $\rightarrow$ ^{136}Te) using the nuclear shell model. Then, we will calculate the nuclear matrix element $M^{0\nu}$ in order to quantify the $M^{0\nu}_{\text{usoft}}/M^{0\nu}$ ratio and check the estimation given in [9].

We will study the use of different interactions in shell model calculations and its impact in the results. We will also discuss the systematics of the $M^{0\nu}_{\text{usoft}}/M^{0\nu}$ ratio along isotopic chains to estimate the NME value for computationally demanding decays like ^{128}Te $\rightarrow$ ^{128}Xe and ^{130}Te $\rightarrow$ ^{130}Xe.

To close this chapter, we will study the $2\nu\beta\beta$ decay amplitude, as it is calculated using the same transition matrix elements as $M^{0\nu}_{\text{usoft}}$ but through a different energy-dependent weighted sum. Thus, we will compare the energies of the intermediate states to which the two cases are most sensitive to.

2.1 Conventional formalism of the $0\nu\beta\beta$ decay amplitude

The rate of the $0\nu\beta\beta$ decay can be calculated using the second order Fermi's Golden rule [18]:

$$d\Gamma^{0\nu} = 2\pi \sum_{spin} |R^{0\nu}|^2 \delta(E_1 + E_2 + E_f - E_i) d\Omega_{e_1} d\Omega_{e_2}, \tag{22}$$

where $\Gamma^{0\nu} = \ln 2 \cdot [T^{0\nu}]^{-1}$, E_1 and E_2 are the energy of the emitted electrons, E_i and E_f are the energies of the initial and final states ($|i\rangle$ and $|f\rangle$) and $R^{0\nu}$ is the transition amplitude [19], that can be expressed as

$$\begin{aligned} R^{0\nu} = & \frac{G_F^2}{8\sqrt{2}\pi R} \int d\mathbf{x} \int d\mathbf{y} (1 - P_{12}) \bar{e}(\varepsilon_1, \mathbf{x}) \gamma_\mu (1 - \gamma_5) \gamma^\mu e^C(\varepsilon_2, \mathbf{y}) \\ & \times g_A^2 \sum_j m_j U_{ej}^2 \\ & \times \frac{R}{g_A^2} \int \frac{d\mathbf{k}}{2\pi^2} \frac{e^{i\mathbf{k}(\mathbf{x}-\mathbf{y})}}{E_\nu} \sum_n \frac{\langle f | J_\mu(\mathbf{x}) | n \rangle \langle n | J^\mu(\mathbf{y}) | i \rangle}{E_\nu + \mu_n - \frac{1}{2}(E_1 - E_2)}, \end{aligned} \tag{23}$$

Looking back to Equation (3), the first line of Equation (23) constitutes the necessary components to calculate the phase space factor $G_{0\nu}(Q_{\beta\beta}, Z)$, the second line is $g_A^2 m_{\beta\beta}$

and the last line corresponds to $M^{0\nu}$, where $R = 1.2A^{1/3}\,\text{fm}$ is the nuclear radius, μ_n is defined as

$$\mu_n \equiv E_n - \frac{1}{2}(E_i + E_f), \tag{24}$$

E_n being the energy of the intermediate state $|n\rangle$, and $E_\nu = \sqrt{m_\nu^2 + \mathbf{k}^2} \sim |\mathbf{k}|$ is the energy of the virtual neutrino. Since nucleons are typically a few fermi apart in nuclei, nuclear wavefunctions will select the preferred momentum for the virtual neutrino to be $|\mathbf{k}| \sim k_F \sim 100\,\text{MeV}$ [19]. This corresponds to the so-called "soft" neutrinos [9], which will constitute the principal contribution to the $0\nu\beta\beta$ decay amplitude. Thus, for light neutrinos in the soft region, $\omega \sim |\mathbf{k}|$ and the dependence on the neutrino mass can be neglected. We can express the momentum integral from Equation (23) in spherical coordinates in order to get rid of the singularity $1/|\mathbf{k}|$ and now having $|\mathbf{k}|$ in the numerator instead.

Additionally, when compared to $|\mathbf{k}|$, $E_1 - E_2$ can be safely neglected (as it can amount up to $Q_{\beta\beta}$ (typically a few MeV) and vanishes on average [19]) and the intermediate energies E_n, which can differ from one another by a few MeV, can be replaced by an average value $\langle E_n \rangle$. This way, we can redefine μ_n to remove its dependence with the intermediate states:

$$\mu_n \simeq \mu \equiv \langle E_n \rangle - \frac{1}{2}(E_i + E_f). \tag{25}$$

Thus, these intermediate states are no longer needed in the calculation, since the closure relation $\sum_n |n\rangle\langle n| = \mathbb{1}$ can be applied to the summation of Equation (23) such that

$$\begin{aligned} \sum_n \frac{\langle f|J_\mu(\mathbf{x})|n\rangle\langle n|J^\mu(\mathbf{y})|i\rangle}{E_\nu + \mu_n - \frac{1}{2}(E_1 - E_2)} &\simeq \frac{1}{|\mathbf{k}| + \mu} \sum_n \langle f|J_\mu(\mathbf{x})|n\rangle\langle n|J^\mu(\mathbf{y})|i\rangle \\ &= \frac{1}{|\mathbf{k}| + \mu} \sum_n \langle f|J_\mu(\mathbf{x})J^\mu(\mathbf{y})|i\rangle. \end{aligned} \tag{26}$$

where $J^\mu(\mathbf{x})$ is the hadronic nuclear current

$$J^\mu(\mathbf{x}) = \sum_i^A \tau_i^+ \left[g^{\mu 0} J_i^0(\mathbf{k}^2) + g^{\mu j}\mathbf{J}_i^j(\mathbf{k}^2)\right] \delta(\mathbf{x} - \mathbf{r}_i), \tag{27}$$

with

$$J_i^0(k^2) = g_V(\mathbf{k}^2), \tag{28}$$

$$\mathbf{J}_i^j(\mathbf{k}^2) = i g_M(\mathbf{k}^2)\frac{\boldsymbol{\sigma}_i \times \mathbf{k}}{2m_N} + g_A(\mathbf{k}^2)\boldsymbol{\sigma}_i - g_P(\mathbf{k}^2)\frac{\mathbf{k}(\mathbf{k}\cdot\boldsymbol{\sigma}_i)}{2m_N}, \tag{29}$$

where m_N is the nucleon mass and $g_M(\mathbf{k}^2)$ and $g_P(\mathbf{k}^2)$ are hadronic couplings.

By substituting these hadronic currents, the expressions of the Gamow-Teller, Fermi and tensor components of the nuclear matrix element $M^{0\nu}$ are given by

$$M^{0\nu}_{GT} = \frac{2R}{\pi g_A^2}\int_0^\infty |\mathbf{k}|\, d|\mathbf{k}| \langle f| \sum_{a,b} \frac{j_0(|\mathbf{k}|r_{ab}) h_{GT}(|\mathbf{k}|)\boldsymbol{\sigma}_a \cdot \boldsymbol{\sigma}_b}{|\mathbf{k}| + \mu} \tau_a^+ \tau_b^+ |i\rangle, \tag{30}$$

$$M^{0\nu}_{F} = \frac{2R}{\pi g_A^2}\int_0^\infty |\mathbf{k}|\, d|\mathbf{k}| \langle f| \sum_{a,b} \frac{j_0(|\mathbf{k}|r_{ab}) h_{F}(|\mathbf{k}|)}{|\mathbf{k}| + \mu} \tau_a^+ \tau_b^+ |i\rangle, \tag{31}$$

$$M^{0\nu}_{T} = \frac{2R}{\pi g_A^2}\int_0^\infty |\mathbf{k}|\, d|\mathbf{k}| \langle f| \sum_{a,b} \frac{j_2(|\mathbf{k}|r_{ab}) h_{T}(|\mathbf{k}|)\left[3\boldsymbol{\sigma}_j \cdot \hat{r}_{ab}\boldsymbol{\sigma}_k \cdot \hat{r}_{ab} - \boldsymbol{\sigma}_a \cdot \boldsymbol{\sigma}_b\right]}{|\mathbf{k}| + \mu} \tau_a^+ \tau_b^+ |i\rangle, \tag{32}$$

where τ^+ is the isospin raising operator, j_0 and j_2 are spherical Bessel functions, $r_{ab} = |\mathbf{r}_a - \mathbf{r}_b|$ is the module of the inter-nucleon position vector whose unit vector is $\hat{r}_{ab} = |\mathbf{r}_a - \mathbf{r}_b|/r_{ab}$ and the h parameters are called the neutrino potentials, defined in momentum space as

$$h_{GT}(|\mathbf{k}|) \equiv g_A^2(\mathbf{k}^2) - \frac{g_A^2(\mathbf{k}^2) g_P^2(\mathbf{k}^2)\mathbf{k}^2}{3m_N} + \frac{g_P^2(\mathbf{k}^2)\mathbf{k}^4}{12m_N^2} + \frac{g_M^2(\mathbf{k}^2)\mathbf{k}^2}{6m_N^2}, \tag{33}$$

$$h_{F}(|\mathbf{k}|) \equiv \frac{g_V^2(\mathbf{k}^2)}{g_A^2}, \tag{34}$$

$$h_{T}(|\mathbf{k}|) \equiv \frac{g_A^2(\mathbf{k}^2) g_P^2(\mathbf{k}^2)\mathbf{k}^2}{3m_N} - \frac{g_P^2(\mathbf{k}^2)\mathbf{k}^4}{12m_N^2} + \frac{g_M^2(\mathbf{k}^2)\mathbf{k}^2}{12m_N^2}. \tag{35}$$

2.2 Contribution of ultrasoft neutrinos ($|\mathbf{k}| \ll k_F$)

In the previous section, we mentioned how neutrinos in the "soft" region ($|\mathbf{k}| \ll k_F \sim 100\,\text{MeV}$) constitute the principal contribution to the $0\nu\beta\beta$ decay amplitude. However, because of the treatment given to the momentum integral in Equation (23), $|\mathbf{k}|$ appears in the numerator (Equations (30), (31) and (32)), suppressing the contribution of low-momentum neutrinos. This is known as the "ultrasoft" region ($|\mathbf{k}| \ll k_F$), and it might carry a non-negligible contribution to the $0\nu\beta\beta$ decay amplitude that we are ignoring as a consequence of how we expressed the momentum integral. In addition, for ultrasoft neutrinos, the approximations performed in Equation (26) are no longer valid ($|\mathbf{k}| \ll 100\,\text{MeV}$). Thus, the intermediate states of the transition play a role when calculating the ultrasoft contribution to the $0\nu\beta\beta$ amplitude.

In a recent article, V. Cirigliano et al. deal with the $0\nu\beta\beta$ decay in chiral effective field theory (χEFT) [9], and obtain expressions for this contribution for the first time. The $0\nu\beta\beta$ transition amplitude is modified as

$$\begin{aligned} R^{0\nu} = {} & \frac{G_F^2}{8\sqrt{2}\pi R}\int d\mathbf{x}\int d\mathbf{y}(1 - P_{12})\bar{e}(\varepsilon_1, \mathbf{x})\gamma_\mu(1 - \gamma_5)\gamma^\mu e^C(\varepsilon_2, \mathbf{y}) \\ & \times g_A^2\, m_{\beta\beta}\,(M^{0\nu} + M^{0\nu}_{\text{usoft}}), \end{aligned} \tag{36}$$

The full expression of $M^{0\nu}_{\text{usoft}}$ is

$$\begin{aligned} M_{\text{usoft}} = &- \frac{\pi R}{g_A^2} \sum_n \int \frac{d^{d-1}k}{(2\pi)^{d-1}} \frac{1}{|\mathbf{k}|} \\ &\times \left[\frac{\langle f|J_\mu|n\rangle\langle n|J^\mu|i\rangle}{|\mathbf{k}| + E_2 + E_n - E_i - i\eta} + \frac{\langle f|J_\mu|n\rangle\langle n|J^\mu|i\rangle}{|\mathbf{k}| + E_1 + E_n - E_i - i\eta} \right], \end{aligned} \tag{37}$$

where the hadronic nuclear current for $|\mathbf{k}| \sim 0$ is reduced to

$$J^\mu(\mathbf{x}) = \sum_i^A \tau_i^+ \left[g^{\mu 0} g_V + g^{\mu j} g_A \boldsymbol{\sigma}_i \right] \delta(\mathbf{x} - \mathbf{r}_i). \tag{38}$$

As we explained in section 1.1, the Fermi term can be neglected, only keeping the Gamow-Teller operator. Evaluating the loop integral in dimensional regularization [9], it can be found that

$$\begin{aligned} M_{\text{usoft}}(\mu_{\text{us}}) = \frac{R}{2\pi} \sum_n \langle f|\boldsymbol{\sigma}\tau^+|n\rangle\langle n|\boldsymbol{\sigma}\tau^+|i\rangle \times \Bigg[&(E_2 + E_n - E_i) \left(\ln \frac{\mu_{\text{us}}}{2(E_2 + E_n - E_i)} + 1 \right) \\ &+ (E_1 + E_n - E_i) \left(\ln \frac{\mu_{\text{us}}}{2(E_1 + E_n - E_i)} + 1 \right) \Bigg], \end{aligned} \tag{39}$$

where we define $\boldsymbol{\sigma}\tau^+ \equiv \sum_i \boldsymbol{\sigma}_i \tau_i^+$ and consider the approximation $E_1 = E_2 = Q_{\beta\beta}/2$, where $Q_{\beta\beta}$ is the Q value of the double-beta decay. The reliability of this approximation is discussed in Appendix A.

The ultraviolet divergence and the logarithmic dependence on the renormalization scale μ_{us} can be shown to be reabsorbed by a another term in the double-beta decay hamiltonian [9]. This way, the total amplitude is shown to be independent of μ_{us}, which will in practice can be replaced by a convenient scale such as $\mu_{\text{us}} = m_\pi \sim k_F \sim 100\,\text{MeV}$, where $m_\pi \sim 100\,\text{MeV} <$ is the scale of the pion mass.

In the article [9], the scaling of the relation $M_{\text{usoft}}/M^{0\nu}$ is shown to be of the order

$$\frac{M^{0\nu}_{\text{usoft}}}{M^{0\nu}} \sim \sum_n \frac{\left(\frac{Q_{\beta\beta}}{2} + E_n - E_i \right)}{4k_F} \times \frac{\langle f|\boldsymbol{\sigma}\tau^+|n\rangle\langle n|\boldsymbol{\sigma}\tau^+|i\rangle}{\langle f|\boldsymbol{\sigma}\tau^+\boldsymbol{\sigma}\tau^+|i\rangle}. \tag{40}$$

As we will see in section 2.4, the energy differences $E_n - E_i$ between bound nuclear states have a typical size of $\mathcal{O}(5-10)\,\text{MeV}$ and $Q_{\beta\beta}$ ranges between $\sim 2-4\,\text{MeV}$. The overlap matrix elements will quickly die out for $E_n - E_i > 10\,\text{MeV}$, further reaffirming our choice of the energy difference scale.

Finally, we find the ratio $M_{\text{usoft}}/M^{0\nu} \sim 10^{-2} - 10^{-1}$, meaning that the ultrasoft contribution is between one and two orders down with respect to the soft, leading contribution. This would imply a correction to the NME potentially ranging between 1% and 10%, which should not be neglected if we want more precise values of the NME, as we discussed in section 1.1.

2.3 Numerical calculations of $M^{0\nu}_{\text{usoft}}$ in $\beta\beta$ decaying nuclei

In the following subsections, we will carry out numerical calculations of $M^{0\nu}_{\text{usoft}}$ in experimentally relevant nuclei. In addition, we will check if our results are in agreement with the estimation from χEFT, $M^{0\nu}_{\text{usoft}}/M^{0\nu} \sim 10^{-2}$.

2.3.1 Calculating transition matrix elements

The shell model code ANTOINE [15, 17], described in subsection 1.2.3, provides us with the tools that will allow us to calculate the transition matrix elements $\langle f|\boldsymbol{\sigma}\tau^+|n\rangle\langle n|\boldsymbol{\sigma}\tau^+|i\rangle$. We will use the following method:

- First of all, we will obtain the wavefunctions of the initial and final 0^+ ground states $|i\rangle$ and $|f\rangle$ corresponding to the parent and daughter even-even nuclei by performing a Lanczos calculation, such that

$$H_{\text{eff}}|i\rangle = E^*_i|i\rangle\ ,\ \ H_{\text{eff}}|f\rangle = E^*_f|f\rangle\ , \tag{41}$$

  where E^*_i and E^*_f are the calculated eigenvalues but not the energies we will be using, as we will see in the following subsection.

- We will apply the Gamow-Teller operator to the initial state $|i\rangle$. The output of this step will be a new state that we will call $|\text{GT}, i\rangle$ and a normalization constant N_i such that

$$\boldsymbol{\sigma}\tau^+|i\rangle = N_i|\text{GT}, i\rangle. \tag{42}$$

- Next, in order to find a set of 1^+ states of the intermediate odd-odd nucleus ($|n\rangle$), we will carry out a Lanczos calculation using the previously obtained $|\text{GT}, i\rangle$ as the pivot. This will provide us with a chosen number (n_{max}) of $|n\rangle$ states, as well as the overlaps of these intermediate states with $|\text{GT}, i\rangle$ (that is, $\langle n|\text{GT}, i\rangle$). Since the $|n\rangle$ states we are interested on are the ones that contribute the most to our calculation, we will keep those that provide a higher value of the $\langle n|\text{GT}, i\rangle$ overlap. As a side note, in this particular calculation, we projected the Lanczos vectors on $\mathbf{J}^2$ in order suppress the emergence of spurious intermediate states with $J \neq 1$.

- Analogously to what we did with the initial state, we will then apply the Gamow-Teller operator to $|f\rangle$ in order to obtain $|\text{GT}, f\rangle$ as well as N_f, such that

$$\boldsymbol{\sigma}\tau^+|f\rangle = N_f|\text{GT}, f\rangle. \tag{43}$$

- Last, we will calculate the overlaps of the $n_{\max}$ $|n\rangle$ states with $|\mathrm{GT}, f\rangle$, obtaining $\langle n|\mathrm{GT}, f\rangle$. With this, we have everything we need to calculate the $(n_{\max})$ overlap matrix elements as

$$\langle f|\boldsymbol{\sigma}\tau^+|n\rangle\langle n|\boldsymbol{\sigma}\tau^+|i\rangle = N_i\, N_f \langle f, \mathrm{GT}|n\rangle\langle n|\mathrm{GT}, i\rangle. \tag{44}$$

It is important to note that Equation (36) takes into account the complete set of infinite $|n\rangle$ intermediate states. As we obviously cannot carry out infinite calculations, we will need to find an appropriate value of $n_{\max}$ that guarantees the convergence of the result.

As an additional check,

$$S(n_{\max}) \equiv \sum_{n=1}^{n_{\max}} \langle f|\boldsymbol{\sigma}\tau^+|n\rangle\langle n|\boldsymbol{\sigma}\tau^+|i\rangle \tag{45}$$

should converge towards

$$S_{fi} \equiv \langle f|\boldsymbol{\sigma}\tau^+\boldsymbol{\sigma}\tau^+|i\rangle = N_i\, N_f \langle f, \mathrm{GT}|\mathrm{GT}, i\rangle\ , \tag{46}$$

since the closure relation $\sum_n |n\rangle\langle n| = \mathbb{1}$ implies

$$\sum_{n=1}^{n_{\max}} |n\rangle\langle n| \xrightarrow{n_{\max}\to\infty} \mathbb{1}. \tag{47}$$

2.3.2 Calculating $M^{0\nu}_{\mathrm{usoft}}$

With the transition matrix elements we just calculated, we only need the corresponding energies from Equation (36) in order to obtain values for $M^{0\nu}_{\mathrm{usoft}}$.

We will calculate the energy of the initial state (E_i) using the binding energies per nucleon (B/A) that can be found in [20, 21]. This way,

$$E_i = Zm_p + Nm_n - (B/A)_{{}^{\mathrm{A}}_{\mathrm{Z}}\mathrm{W}} \cdot A\ , \tag{48}$$

where ${}^{\mathrm{A}}_{\mathrm{Z}}\mathrm{W}$ is the parent nucleus.

To calculate the ground state energy of the intermediate states (that is, the energy of the lowest-lying intermediate state, $E_{1^+_1}$), we will also need an $E^{\mathrm{GS}\to 1^+_1}$ excitation energy, which we will be taking from [22]. So, it follows that

$$E_{1^+_1} = (Z+1)m_p + (N-1)m_n - (B/A)_{{}^{\mathrm{A}}_{\mathrm{Z+1}}\mathrm{X}} \cdot A + E^{\mathrm{GS}\to 1^+_1}_{{}^{\mathrm{A}}_{\mathrm{Z+1}}\mathrm{X}}\ , \tag{49}$$

where ${}^{A}_{Z+1}\mathrm{X}$ is the intermediate nucleus.

For experimentally observed double-beta decays, we will take $Q_{\beta\beta}$ from the literature [23, 24]. Otherwise, we will simply take

$$Q_{\beta\beta} = E_i - E_f - 2m_e = 2(m_n - m_p) + [(B/A)_{{}^{A}_{Z+2}\mathrm{Y}} - (B/A)_{{}^{A}_{Z}\mathrm{W}}] - 2m_e \,, \tag{50}$$

where

$$E_f = (Z+2)m_p + (N-2)m_n - (B/A)_{{}^{A}_{Z+2}\mathrm{Y}} \cdot A \,; \tag{51}$$

${}^{A}_{Z+2}\mathrm{Y}$ being the daughter nucleus. Now that we have everything we need to calculate $M^{0\nu}_{\mathrm{usoft}}$, we will begin by representing $S(n_{\max})$ for a certain range of values of $n_{\max}$ in order to find an appropriate $n_{\max}$ that guarantees the convergence $S(n_{\max}) \to S_{fi}$, as we discussed in the previous subsection (2.3.1).

In Figures 4 and 5 we have represented $S(n_{\max})$ with $10 \leq n_{\max} \leq 60$ for the double-beta decay of ^{48}Ca and ^{136}Xe using the KB3 and GCN5082 interaction, respectively. As we can see, $S(n_{\max})$ is well converged to S_{fi} for $n_{\max} = 60$. We can also appreciate this convergence if we represent $M^{0\nu}_{\mathrm{usoft}}$ as a function of $n_{\max}$, as shown in Figures 6 and 7.

As a note, we have performed this convergence check for all nuclei and interactions considered in this chapter. For the sake of brevity, we will present its corresponding figures in Appendix B (Figures 25-30).

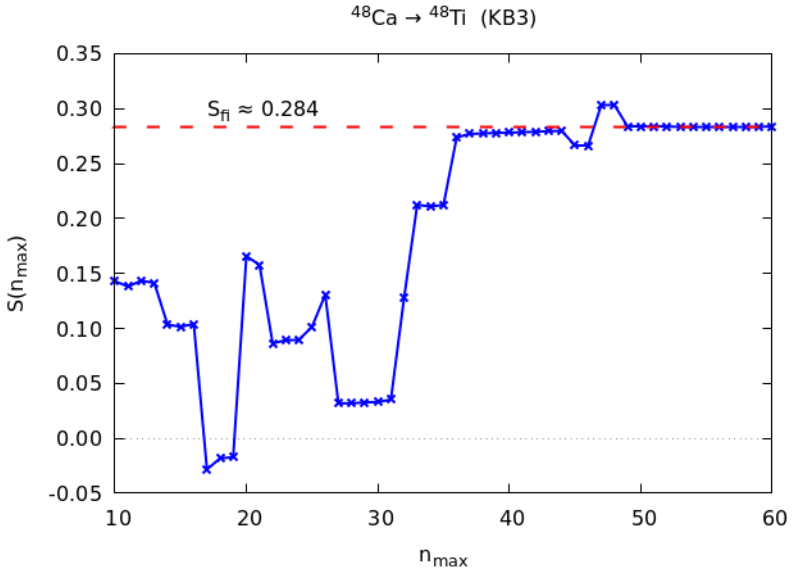

Figure 4: $S(n_{\max})$ for the double-beta decay of ^{48}Ca, using the KB3 interaction. The value of S_{fi} is depicted with a red dashed line.

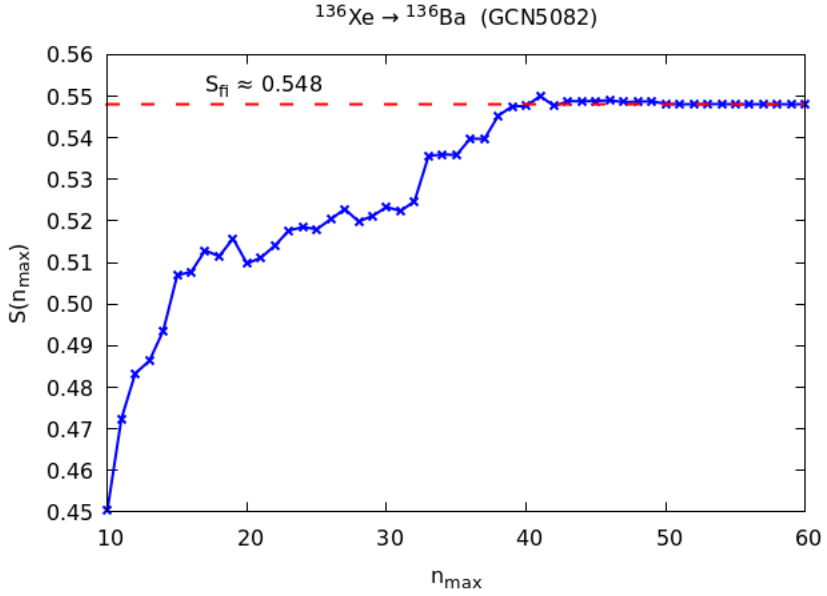

Figure 5: $S(n_{\max})$ for the double-beta decay of ^{136}Xe, using the GCN5082 interaction.

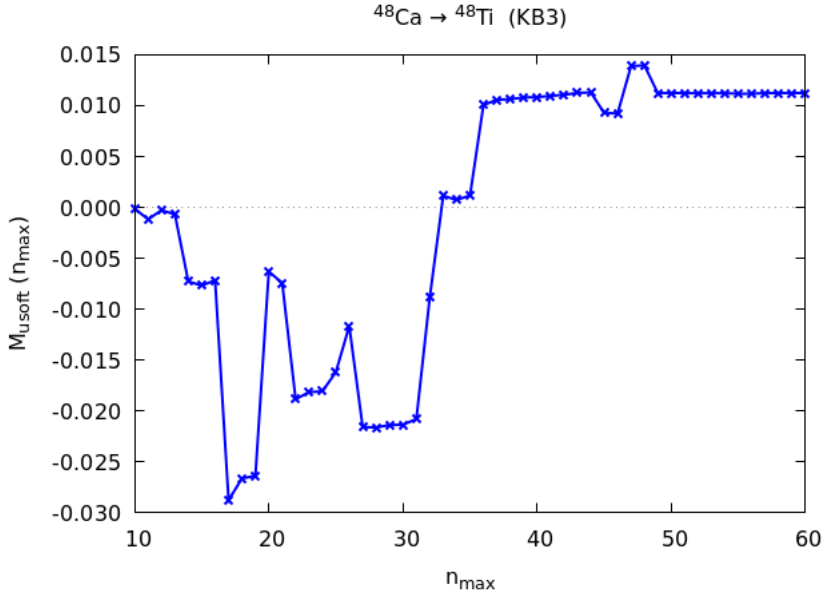

Figure 6: Matrix element $M^{0\nu}_{\text{usoft}}$ with respect to the number 1^+ of intermediate states $n_{\max}$ for the double-beta decay of ^{48}Ca, using the KB3 interaction.

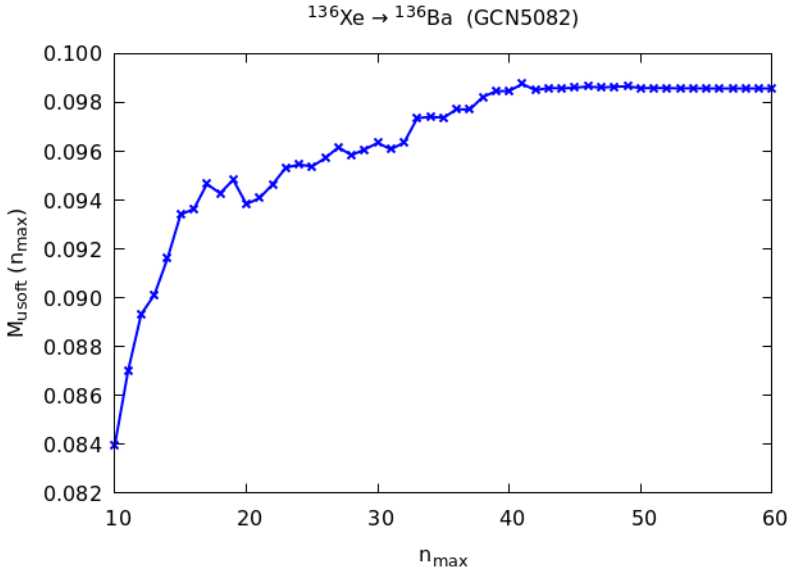

Figure 7: Matrix element $M^{0\nu}_{\text{usoft}}$ with respect to the number 1^+ of intermediate states n_{max} for the double-beta decay of ^{136}Xe, using the GCN5082 interaction.

Thus, we will calculate $M^{0\nu}_{\text{usoft}}$ for two different experimentally observed double-beta decaying nuclei: ^{48}Ca, where we will work in the valence space consisting on $0f_{7/2}$, $1p_{3/2}$, $0f_{5/2}$ and $1p_{1/2}$ (also known as the pf-shell), using the KB3 interaction; and ^{136}Xe, working in the $0g_{7/2}$, $1d_{5/2}$, $1d_{3/2}$, $2s_{1/2}$ and $0h_{11/2}$ valence space and using the GCN5082 interaction. The results are presented in Table 1 below.

Now, in order to calculate the $M^{0\nu}_{\text{usoft}}/M^{0\nu}$ ratio, we will use the shell model code NATHAN. Since the intermediate 1^+ states do not play any role in the calculation, only $J = 0$ states will be involved, an optimal condition for J-coupled scheme code like NATHAN, as we discussed in subsection 1.2.3.

Parent	Interaction	E_i (MeV)	$E_{1^+_1}$ (MeV)	E_f (MeV)	$Q_{\beta\beta}$ (MeV)	$M^{0\nu}_{\text{usoft}}$
^{48}Ca	KB3	44657.259	44658.669	44651.970	4.263 [23]	$1.12 \cdot 10^{-2}$
^{136}Xe	GCN5082	126569.136	126569.306	126565.657	2.458 [24]	$9.86 \cdot 10^{-2}$

Table 1: Energies, $Q_{\beta\beta}$ value and $M^{0\nu}_{\text{usoft}}$ (calculated for $n_{\text{max}} = 60$) for the $\beta\beta$ emitters ^{48}Ca and ^{136}Xe. The energies E_i, $E_{n,GS}$ and E_f are taken from [20, 21, 22].

Parent	Interaction	$M^{0\nu}_{\text{usoft}}$	$M^{0\nu}$	$M^{0\nu}_{\text{usoft}}/M^{0\nu}$
^{48}Ca	KB3	$1.12 \cdot 10^{-2}$	0.93	$1.2 \cdot 10^{-2}$
^{136}Xe	GCN5082	$9.86 \cdot 10^{-2}$	2.30	$4.3 \cdot 10^{-2}$

Table 2: $M^{0\nu}_{\text{usoft}}$, $M^{0\nu}$ and its ratio for the $0\nu\beta\beta$ decay of ^{48}Ca and ^{136}Xe.

As we can see, the ratio $M^{0\nu}_{\text{usoft}}/M^{0\nu} \sim 10^{-2}$ holds up for both of the calculated cases. In particular, the ultrasoft contribution for the $0\nu\beta\beta$ decay of ^{48}Ca and ^{136}Xe represents a correction to the conventional NME of around 1.2% and 4.3% respectively. This, in turn, implies a correction to the $0\nu\beta\beta$ decay rate (Equation (3)) of $\sim 2.4\%$ and $\sim 8.6\%$, which should not be neglected if one wants precise values of the NME.

2.3.3 Sensitivity of $M^{0\nu}_{\text{usoft}}$ to the nuclear interaction

In the previous subsection, for the calculations involving the double-beta decay of ^{136}Xe, we used the GCN5082 interaction, which is an effective hamiltonian based in a renormalized G-matrix obtained from the Bonn-C potential and constructed through a fit to about 300 energy levels from ~ 90 nuclei [25], making it a more realistic and sophisticated interaction.

However, it might be interesting to repeat the calculations using three different G-matrices based on the different Bonn potentials to see how much they differ from the GCN5082 calculations. In Table 3 below, we present the calculated values of $M^{0\nu}_{\text{usoft}}$, $M^{0\nu}$ and its ratio using these Bonn interactions (A through C), including the previously calculated case for the GCN5082 interaction.

Parent	Interaction	$M^{0\nu}_{\text{usoft}}$	$M^{0\nu}$	$M^{0\nu}_{\text{usoft}}/M^{0\nu}$
^{136}Xe	Bonn-A	$2.88 \cdot 10^{-2}$	1.11	$2.6 \cdot 10^{-2}$
^{136}Xe	Bonn-B	$3.52 \cdot 10^{-2}$	1.18	$3.0 \cdot 10^{-2}$
^{136}Xe	Bonn-C	$4.05 \cdot 10^{-2}$	1.25	$3.2 \cdot 10^{-2}$
^{136}Xe	GCN5082	$9.86 \cdot 10^{-2}$	2.30	$4.3 \cdot 10^{-2}$

Table 3: $M^{0\nu}_{\text{usoft}}$, $M^{0\nu}$ and its ratio for the $0\nu\beta\beta$ decay of ^{136}Xe using different nuclear interactions.

Table 3 shows that the results are pretty similar for the three variants of the Bonn interaction. Even though both $M^{0\nu}_{\text{usoft}}$ and $M^{0\nu}$ increase by around a factor 2 for the GCN5082 interaction with respect to Bonn-C, the ratio between the two values roughly stays the same for all interactions, leading to a very robust $M^{0\nu}_{\text{usoft}}$ correction.

2.3.4 Computationally complex nuclei: $0\nu\beta\beta$ decay of ^{128}Te and ^{130}Te

In addition to ^{48}Ca and ^{136}Xe, we would have also wanted to study other experimentally observed double-beta decaying nuclei, like ^{128}Te and ^{130}Te.

However, as we mentioned in subsection 1.2.3, the dimension of the many-body matrix increases proportionally to the product of two binomial coefficients that depend on the total degeneracy of the valence spaces and the number of valence nucleons.

The maximum dimension that can be handled by the version of ANTOINE we used is $N_{\text{dim,max}} = 2 \cdot 10^8$, while the dimensions of the matrices needed to calculate the daughter nuclei ^{128}Xe and ^{130}Xe are

$$N_{\text{dim}}(^{128}\text{Xe}) = \binom{32}{4} \cdot \binom{32}{24} \sim 4 \cdot 10^{11} \,, \tag{52}$$

$$N_{\text{dim}}(^{130}\text{Xe}) = \binom{32}{4} \cdot \binom{32}{26} \sim 3 \cdot 10^{10} \,. \tag{53}$$

We could, however, do a preliminary study and carry out calculations for similar nuclei that are computationally feasible (like ^{132}Te and ^{134}Te) in order to check how the relative contribution of $M^{0\nu}_{\text{usoft}}$ varies along an isotopic chain.

To do this, we will first study Ca isotopes around ^{48}Ca like ^{46}Ca and ^{50}Ca using the same nuclear interaction.

Parent	Interaction	$Q_{\beta\beta}$ (MeV)	$M^{0\nu}_{\text{usoft}}$	$M^{0\nu}$	$M^{0\nu}_{\text{usoft}}/M^{0\nu}$
^{46}Ca	KB3	0.988 [20, 21]	$1.04 \cdot 10^{-2}$	1.20	$8.7 \cdot 10^{-3}$
^{48}Ca	KB3	4.263 [23]	$1.12 \cdot 10^{-2}$	0.929	$1.2 \cdot 10^{-2}$
^{50}Ca	KB3	5.921 [20, 21]	$9.97 \cdot 10^{-4}$	1.063	$9.4 \cdot 10^{-4}$

Table 4: $M^{0\nu}_{\text{usoft}}$, $M^{0\nu}$ and its ratio for different Ca isotopes, alongside it's $Q_{\beta\beta}$ value.

Table 4 shows that the obtained values of $M^{0\nu}_{\text{usoft}}$ are reasonably similar for ^{46}Ca and ^{48}Ca, but decrease an order of magnitude for ^{50}Ca. However, as can be seen in Figures 4, 6, 27 and 28, the individual contributions of each term in the summation are comparable for the three cases, with the exception that, for ^{50}Ca, they cancel each other more often, resulting in an overall lower total value.

Therefore, our results suggest that calculations for certain nuclei can qualitatively give us an idea of the results for similar isotopes.

Parent	Interaction	$Q_{\beta\beta}$ (MeV)	$M^{0\nu}_{\text{usoft}}$	$M^{0\nu}$	$M^{0\nu}_{\text{usoft}}/M^{0\nu}$
^{132}Te	GCN5082	4.090 [20, 21]	$6.34 \cdot 10^{-2}$	2.55	$2.5 \cdot 10^{-2}$
^{134}Te	GCN5082	5.592 [20, 21]	$8.58 \cdot 10^{-2}$	1.94	$4.4 \cdot 10^{-2}$

Table 5: $M^{0\nu}_{\text{usoft}}$, $M^{0\nu}$ and its ratio for different Te isotopes, alongside it's $Q_{\beta\beta}$ value.

Table 5 shows the results for ^{132}Te and ^{134}Te, which are comparable to those obtained for ^{136}Xe. As such, we can expect a similar contribution of $M^{0\nu}_{\text{usoft}}$ for the $0\nu\beta\beta$ decay of ^{128}Te and ^{130}Te.

2.4 Energy dependence: comparison to $2\nu\beta\beta$ decay

The transition matrix elements $\langle f|J_\mu|n\rangle\langle n|J^\mu|i\rangle$ from Equation (36) that we calculated in the previous subsections also control the $2\nu\beta\beta$ decay amplitude, although through a different E_n-dependent weighted sum [9].

In particular, the Gamow-Teller matrix element $M^{2\nu}_{GT}$ [26] can be written as

$$M^{2\nu}_{GT} = m_e \sum_n \frac{\langle f|\boldsymbol{\sigma}\tau^+|n\rangle\langle n|\boldsymbol{\sigma}\tau^+|i\rangle}{E_n - (E_i + E_f)/2}. \tag{54}$$

We will analyze the dependence with respect to E_n of $M^{2\nu}_{GT}$ and $M^{0\nu}_{\text{usoft}}$. In particular, we will represent the running sum with respect to the energy difference between the corresponding intermediate state and the initial state, $E_n - E_i$. This way, we can visualize the contribution of each state to $M^{2\nu}_{GT}$ and $M^{0\nu}_{\text{usoft}}$. We define

$$S^{2\nu}_{GT}(n) = m_e \frac{\langle f|\boldsymbol{\sigma}\tau^+|n\rangle\langle n|\boldsymbol{\sigma}\tau^+|i\rangle}{E_n - (E_i + E_f)/2}, \tag{55}$$

$$S^{0\nu}_{\text{usoft}}(n) = \frac{R}{2\pi}\langle f|\boldsymbol{\sigma}\tau^+|n\rangle\langle n|\boldsymbol{\sigma}\tau^+|i\rangle \times 2\left(\frac{Q_{\beta\beta}}{2} + E_n - E_i\right)\left(\ln\frac{m_\pi}{2\left(\frac{Q_{\beta\beta}}{2} + E_n - E_i\right)} + 1\right), \tag{56}$$

such that $M^{2\nu}_{GT} = \sum_n S^{2\nu}_{GT}(n)$ and $M^{0\nu}_{\text{usoft}} = \sum_n S^{0\nu}_{\text{usoft}}(n)$.

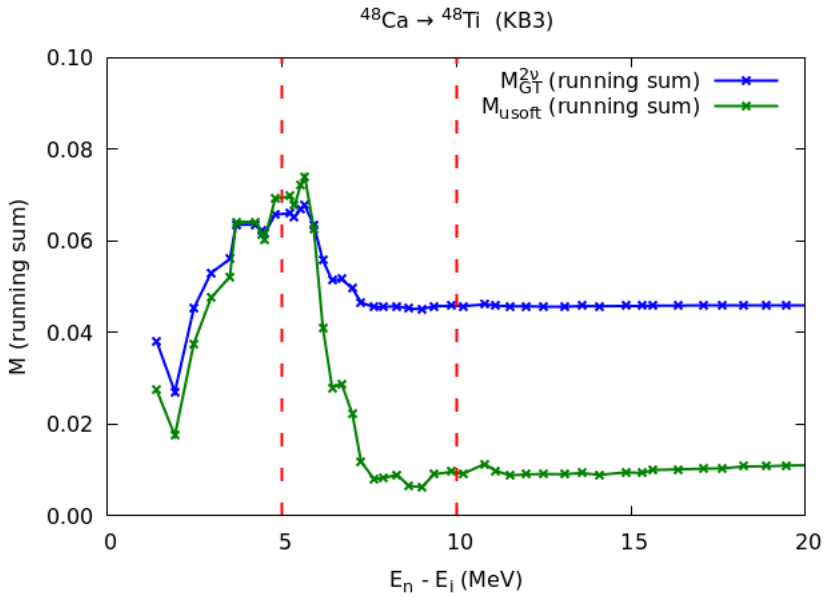

Figure 8: Running sum of $M^{2\nu}_{GT}$ and $M^{0\nu}_{\text{usoft}}$ with respect to $E_n - E_i$ for the double-beta decay of ^{48}Ca, using the KB3 interaction.

Figure 8 shows that, as expected due to its dependence on E_n, $M^{2\nu}_{GT}$ is more sensitive to low-energy intermediate states ($E_n - E_i < 5\,\text{MeV}$) than to the ones with a higher energy difference like those in the $5\,\text{MeV} < E_n - E_i < 10\,\text{MeV}$ region (depicted between red dashed lines for clarity). This implies higher values of $S^{2\nu}_{GT}(n)$ for the low-energy region and thus a more abrupt change in the value of the running sum. After that, the values of $S^{2\nu}_{GT}(n)$ practically vanish for $E_n - E_i > 10\,\text{MeV}$.

On the other hand, and following the same reasoning, $M^{0\nu}_{\text{usoft}}$ is much more sensitive to states in the $5\,\text{MeV} < E_n - E_i < 10\,\text{MeV}$ region than $M^{2\nu}_{GT}$, after which $S^{0\nu}_{\text{usoft}}(n)$ also rapidly decays for high energies.

This is even clearer for the double-beta decay of ^{136}Xe. In Figure 9 we can distinguish how $M^{0\nu}_{\text{usoft}}$ is more sensitive to states between $5\,\text{MeV} < E_n - E_i < 10\,\text{MeV}$ than $M^{2\nu}_{GT}$.

This is consistent with the estimation of subsection 2.1, where we said that the energy differences $E_n - E_i$ between bound nuclear states have a typical size of $\mathcal{O}(5-10)\,\text{MeV}$, while the transition matrix elements $\langle f|J_\mu|n\rangle\langle n|J^\mu|i\rangle$ (and, consequently, $S^{2\nu}_{GT}(n)$ and $S^{0\nu}_{\text{usoft}}(n)$) rapidly die out for $E_n - E_i > 10\,\text{MeV}$.

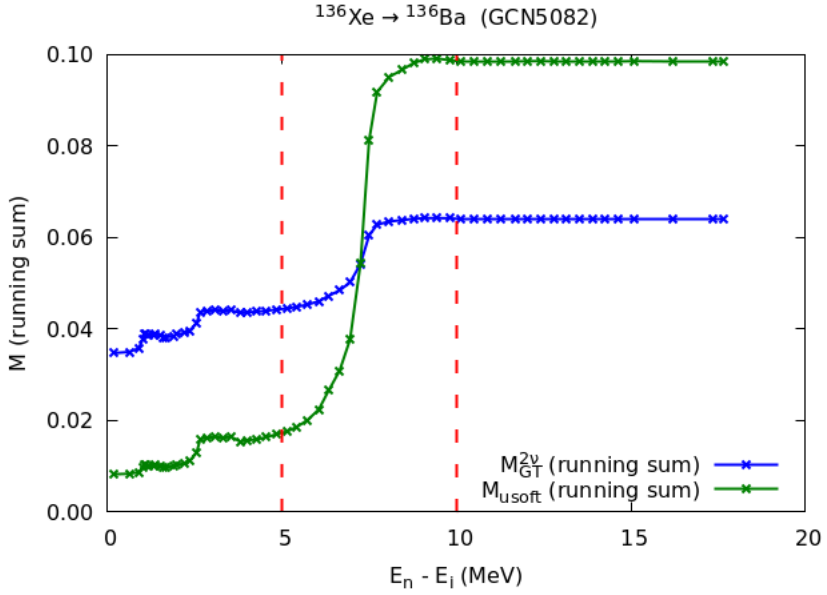

Figure 9: Running sum of $M^{2\nu}_{GT}$ and $M^{0\nu}_{\text{usoft}}$ with respect to $E_n - E_i$ for the double-beta decay of ^{136}Xe, using the GCN5082 interaction.

3 Realistic radial wavefunctions in NME calculations

In order to solve $H_{\text{eff}}|\Psi_{\text{eff}}\rangle = E|\Psi_{\text{eff}}\rangle$, the radial part of the wavefunctions is not explicitly assumed, since only matrix elements of H_{eff} are needed and Ψ_{eff} is given as a combination of Slater determinants. However, in order to evaluate NME of r-dependent operators, the explicit form of the radial wavefunction is needed. While the harmonic oscillator is the conventional choice, it might be too simple if we want to obtain accurate results.
In the following chapter we will study the impact of realistic radial wavefunctions on the value of nuclear matrix elements, as well as the choice of the valence space. In particular, we will present the differences between harmonic oscillator and Woods-Saxon radial wavefunctions and compare them to the results obtained through the more accurate variational Monte Carlo (VMC) calculations.
Following an article by X.B. Wang et al. [27], we will study the effects of these radial wavefunctions towards the calculation of the NME of the double-beta decay of light nuclei ($A = 10$ and $A = 12$), as well as the differences that arise from using a simple valence space (like the p-shell) or an extended valence space (psd-shell). We extend this study taking into account all three contributions to $M^{0\nu}$ ($M_F^{0\nu}$, $M_{GT}^{0\nu}$ and $M_T^{0\nu}$, the last of which is neglected) in order to produce a more accurate result. In addition, for the first time we extend this study towards the double-beta decay of heavier nuclei ($A = 48$).

3.1 Harmonic oscillator wavefunctions

Typically, instead of going through the steps that lead to self-consistency, one simply selects a particular type of mean-field potential. The use of such phenomenological potentials is a practical shortcut taken at the expense of theoretical preciseness [28].

The simplest frequently used potential is the three-dimensional harmonic oscillator (HO) potential:

$$v_{HO}(r) = -V_1 + kr^2 = -V_1 + \frac{1}{2}m_N\omega^2 r^2, \tag{57}$$

where V_1 and k are parameters to be fitted for best results. Given this potential, the harmonic oscillator wavefunctions $g_{nl}(r)$ are solutions of the radial Schrödinger equation

$$\frac{-\hbar^2}{2m_N}\left[\nabla_r^2 - \frac{l(l+1)}{r^2}\right] g_{nl}(r) + \left(-V_1 + \frac{1}{2}m_N\omega^2 r^2\right) g_{nl}(r) = \varepsilon_{nl} g_{nl}(r), \tag{58}$$

where

$$2n + l = N = 0, 1, 2, 3, ... \tag{59}$$

are the radial quantum numbers and

$$\varepsilon_{nl} = -V_1 + \left(N + \frac{3}{2}\right)\hbar\omega = -V_1 + \left(2n + l + \frac{3}{2}\right)\hbar\omega \tag{60}$$

are the energy eigenvalues.
As we previously mentioned in section 1.2, we will be using the convention where the principal quantum number $n = 0, 1, 2, 3, ...$ indicates the number of nodes of the wavefunction.

The HO radial wavefunction can explicitly be written as [29]

$$g_{nl}(r) = \sqrt{\frac{2n!}{b^3\Gamma(n + l + \frac{3}{2})}} \left(\frac{r}{b}\right)^l e^{-r^2/2b^2} L_n^{(l+\frac{1}{2})}\left(\frac{r^2}{b^2}\right), \tag{61}$$

where b is the oscillator length and $L_n^{(l+\frac{1}{2})}(x)$ is the associated Laguerre polynomial [30]. The oscillator length, as the name suggests, characterizes the width of the oscillator potential, and it can be expressed as

$$b \equiv \sqrt{\frac{\hbar}{m_N\omega}} = \frac{\hbar c}{\sqrt{(m_N c^2)(\hbar\omega)}} \approx \frac{197.33}{\sqrt{940 \cdot \hbar\omega}}\text{fm}, \tag{62}$$

where we will take the value of $\hbar\omega$ from the Blomqvist-Molinari formula [31], based on a fit to charge radii across the nuclear chart:

$$\hbar\omega = \left(45A^{-1/3} - 25A^{-2/3}\right)\text{MeV}. \tag{63}$$

Instead of directly using the associated Laguerre polynomials, numerical values of $g_{nl}(r)$ can be obtained via auxiliary functions, as we explain in Appendix C. This way, we can generate the HO radial wavefunctions $g_{nl}(r)$, which we can use, for example, to obtain the nucleon density profile (either for protons or neutrons) $\rho(r)$, defined as

$$\rho(r) = |\Psi(r)|^2 = \sum_{nl} a_{nl}^2 \, |g_{nl}(r)|^2, \tag{64}$$

where a_{nl}^2 is the occupancy of orbitals with quantum numbers nl and the sum runs over all orbitals of the inert core and the chosen valence space.

We will use the shell model code NATHAN to calculate these occupancies. Following Wang's paper [27], we will use 2 different valence spaces for the study of light nuclei: the p-shell ($0p_{3/2}$ and $0p_{1/2}$) and the psd-shell ($0p_{3/2}$, $0p_{1/2}$, $0d_{5/2}$, $1s_{1/2}$ and $0d_{3/2}$), where the PSDMWK shell model hamiltonian [32, 33] will be used, adding a correction that takes

into account center-of-mass (CoM) excitations [34] for the *psd*-shell. For example, for the ^{10}Be nucleus, we obtain the occupancies of Table 6 below.

Valence space	Nucleon	$0p_{3/2}$	$0p_{1/2}$	$0d_{5/2}$	$0d_{3/2}$	$1s_{1/2}$
p-shell	Protons	1.7385	0.2615	0.0000	0.0000	0.0000
	Neutrons	3.5119	0.4881	0.0000	0.0000	0.0000
psd-shell	Protons	1.6675	0.2871	0.0140	0.0275	0.0039
	Neutrons	3.2032	0.5732	0.1421	0.0710	0.0105

Table 6: Nucleon occupancies of the ^{10}Be nucleus for calculations in two different valence spaces using the PSDMWK interaction, with a correction that takes into account CoM excitacions for the *psd*-shell case.

The orbitals of the inert core (0s) are full by definition, so its occupancy is trivial: $a^2_{0s} = 2$ for both protons and neutrons. For the time being, since the HO radial wavefunctions do not depend on the total angular momentum quantum number j, we will only care about the occupancies of the nl orbitals, meaning that the *p*-shell occupancy is also trivial: $a^2_{0p} = Z - 2$ for protons and $a^2_{0p} = N - 2$ for neutrons.

Using these occupancies, we can finally obtain the nucleon density profile. This way, we will be able to compare it to the density profile of ^{10}Be obtained through variational Monte Carlo (VMC) [35].

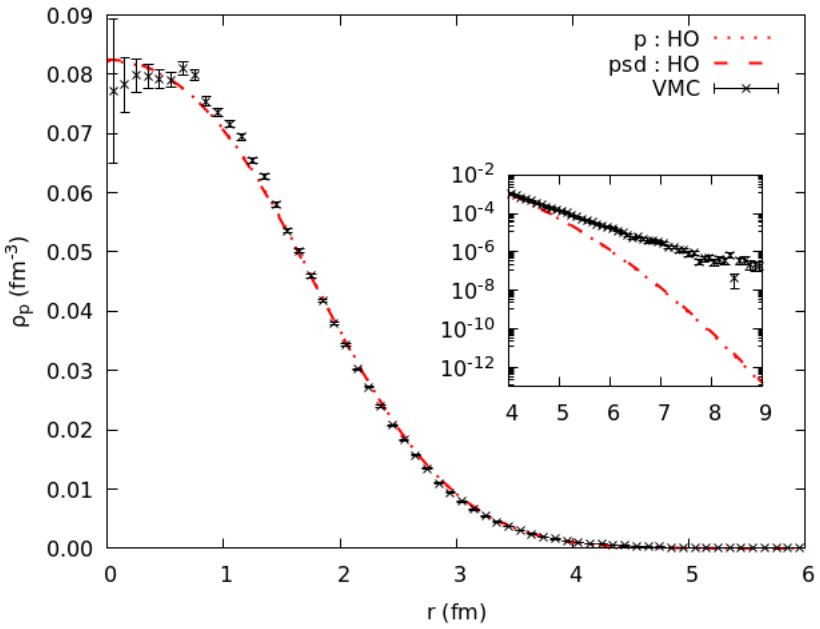

Figure 10: Proton density profile of ^{10}Be. The dotted (dashed) red line corresponds to shell model calculations in the *p*-shell (*psd*-shell) configuration space using HO radial wavefunctions and the black points correspond to VMC calculations [35]. The asymptotic behaviour of the density profile has been included.

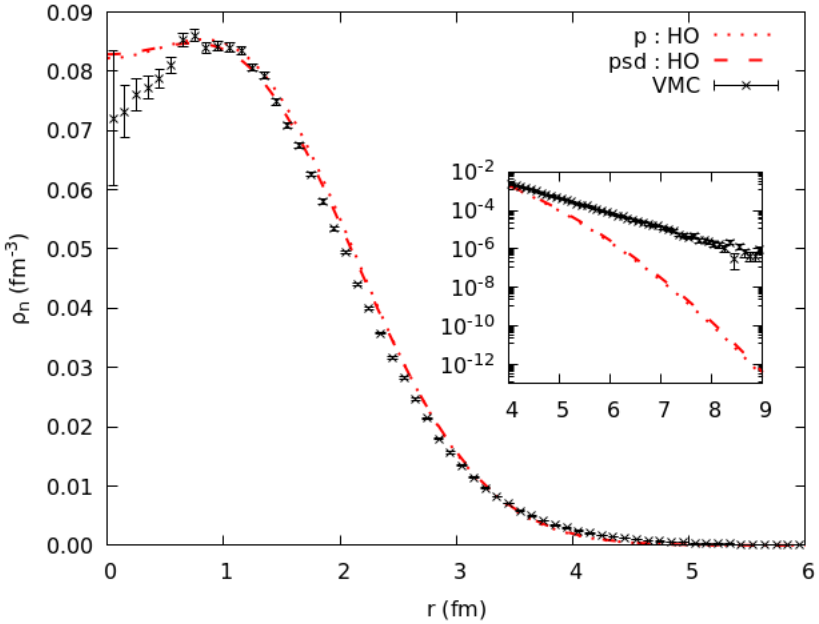

Figure 11: Neutron density profile of ^{10}Be. The dashed red lines correspond to shell model calculations for *p*- and *psd*-shell using HO radial wavefunctions. The black points correspond to VMC calculations.

Figures 10 and 11 show that there are discrepancies at very small $r < 1\,\text{fm}$, but a reasonable agreement at medium values of r. However, if we zoom in for larger values of r, we observe that the HO radial wavefunction dies out way faster than VMC, the latter being a more sophisticated calculation. Consequently, we conclude that the harmonic oscillator does not accurately reproduce asymptotic behaviour; pointing out the need for better, more realistic radial wavefunctions.

3.2 Woods-Saxon wavefunctions

A phenomenological potentials associated with more realistic radial wavefunctions is the Woods-Saxon potential [28]

$$v_{WS}(r) = \frac{-V_0}{1 + e^{(r-R)/a}}. \tag{65}$$

The typically used parametrization [28] is

$$R = r_0 A^{1/3} = 1.27 A^{1/3}\,\text{fm}, \tag{66}$$

$$a = 0.67\,\text{fm}, \tag{67}$$

$$V_0 = \left(51 \pm 33\,\frac{N-Z}{A}\right)\text{MeV}, \tag{68}$$

where R is the nuclear radius, a is known as "surface diffuseness" and the $\pm$ in V_0 is taken as $+$ for protons and $-$ for neutrons. The associated radial Schrödinger equation is

$$\begin{aligned}&\left\{\frac{-\hbar^2}{2m_N}\left[\nabla_r^2-\frac{l(l+1)}{r^2}\right]+v_{WS}(r)+v_C(r)\right.\\&\left.+\frac{1}{2}\left[j(j+1)-l(l+1)-\frac{3}{4}\right]\hbar^2 v_{LS}(r)\right\}f_{nlj}(r)=\varepsilon_{nlj}f_{nlj}(r),\end{aligned}\tag{69}$$

where the Coulomb potential is given by a uniformly charged sphere of radius R for protons

$$v_C(r)=\frac{Ze^2}{4\pi\epsilon_0}\begin{cases}\frac{3-(r/R)^2}{2R}\,, & r\le R\\ \frac{1}{r}\,, & r>R\end{cases}\tag{70}$$

and $v_C(r)=0$ for neutrons; and the spin-orbit potential is taken as

$$v_{LS}(r)=v_{LS}^{(0)}\left(\frac{r_0}{\hbar}\right)^2\frac{1}{r}\left[\frac{d}{dr}\frac{1}{1+e^{(r-R)/a}}\right],\tag{71}$$

with $v_{LS}^{(0)}=0.44V_0$, and $f_{nlj}(r)$ is the Woods-Saxon (WS) radial wavefunction.

As opposed to the HO case, the radial Schrödinger equation cannot be solved analytically for the WS case, and as such $f_{nlj}(r)$ does not have an analytical expression. However, $f_{nlj}(r)$ can be expanded as a linear combination of HO radial wavefunctions $g_{nl}(r)$:

$$f_{nlj}(r)=\sum_\nu A_\nu^{(nlj)}g_{\nu l}(r),\tag{72}$$

with the normalization condition

$$\sum_\nu\left[A_\nu^{(nlj)}\right]^2=1.\tag{73}$$

This way, we will find the solution by constructing the hamiltonian matrix in the HO basis and diagonalizing it. The hamiltonian matrix elements are

$$\langle\nu'|h_{lj}(r)|\nu\rangle\equiv\int_0^\infty r^2\,dr\,g_{\nu' l}(r)h_{lj}(r)g_{\nu l}(r),\tag{74}$$

where $h_{lj}(r)$ is the hamiltonian used in Equation (69). To avoid prior numerical differentiation by the ∇_r^2 term in $h_{lj}(r)$, we will take $\nabla_r^2 g_{nl}(r)$ from the HO equation (58) [28]. This leaves Equation (74) as

$$\begin{aligned}\langle \nu' | h_{lj}(r) | \nu \rangle = \int_0^\infty r^2\, dr\, g_{\nu' l}(r) g_{\nu l}(r) \Bigg\{ & \frac{-\hbar^2}{2m_N b^2} \left[(4n + 2l + 3)\delta_{\nu'\nu} + \left(\frac{r}{b}\right)^2 \right] \\ & + v_{WS}(r) + v_C(r) + \frac{1}{2}\left[j(j+1) - l(l+1) - \frac{3}{4} \right] \hbar^2 v_{LS}(r) \Bigg\}.\end{aligned} \tag{75}$$

Diagonalizing the matrix, we will obtain the eigenvalues ε_{nlj} and the eigenvectors $f_{nlj}(r)$ in the HO basis, thus obtaining the oscillator amplitudes $A_\nu^{(nlj)}$.

Tables 7 and 8 show these oscillator amplitudes for ^{10}Be. Using the shell model occupancies from Table 6, we obtain the WS density profile and compare it to the HO case as well as with the VMC data in Figures 12 and 13.

nlj	ε_{nlj}	$\nu=0$	$\nu=1$	$\nu=2$	$\nu=3$	$\nu=4$	$\nu=5$
$0s_{1/2}$	-28.765	0.999	0.041	0.024	-0.011	-0.002	-0.003
$0p_{3/2}$	-14.653	0.998	0.007	0.064	-0.023	0.005	-0.007
$0p_{1/2}$	-7.522	0.990	-0.068	0.111	-0.040	0.021	-0.012
$0d_{5/2}$	-1.398	0.978	-0.111	0.155	-0.076	0.040	-0.024
$1s_{1/2}$	-0.022	-0.028	0.909	-0.292	0.255	-0.138	0.061
$0d_{3/2}$	6.189	0.768	-0.406	0.372	-0.263	0.172	-0.085

Table 7: Woods-Saxon energies ε_{nlj} and oscillator amplitudes $A_\nu^{(nlj)}$ for proton single-particle states in ^{10}Be, calculated using the WS parameters from Eqs. (66)-(68).

nlj	ε_{nlj}	$\nu=0$	$\nu=1$	$\nu=2$	$\nu=3$	$\nu=4$	$\nu=5$
$0s_{1/2}$	-21.520	0.999	-0.038	0.032	-0.018	0.002	-0.003
$0p_{3/2}$	-8.917	0.987	-0.117	0.095	-0.050	0.019	-0.012
$0p_{1/2}$	-3.852	0.960	-0.205	0.161	-0.086	0.046	-0.023
$0d_{5/2}$	2.145	0.904	-0.292	0.246	-0.160	0.093	-0.048
$1s_{1/2}$	1.736	0.051	0.810	-0.426	0.331	-0.203	0.093
$0d_{3/2}$	6.277	0.667	-0.472	0.421	-0.317	0.209	-0.103

Table 8: Woods-Saxon energies ε_{nlj} and oscillator amplitudes $A_\nu^{(nlj)}$ for neutron single-particle states in ^{10}Be, calculated using the WS parameters from Eqs. (66)-(68).

Tables 7 and 8 show that the main oscillator component for each state corresponds to $\nu = n$. The wavefunctions of the lowest-lying Woods-Saxon states match the corresponding oscillator states to a great degree. Nevertheless, as the energy increases, the other oscillator components ($\nu \neq n$) begin to acquire a non-negligible amplitude, thus deviating from the corresponding HO wavefunction.

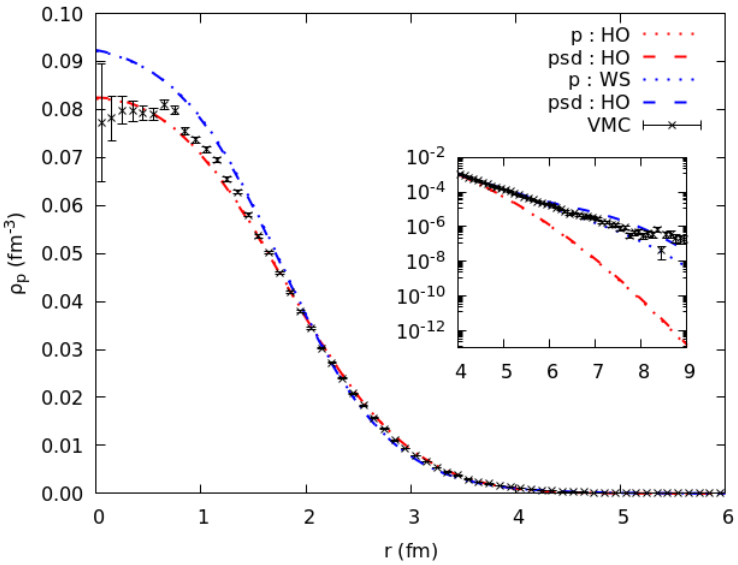

Figure 12: Proton density profile of ^{10}Be. Same as Figure 10, with the addition of shell model calculations in the *p*- and *psd*-shell configuration spaces using WS radial wavefunctions (blue dotted and dashed lines, respectively).

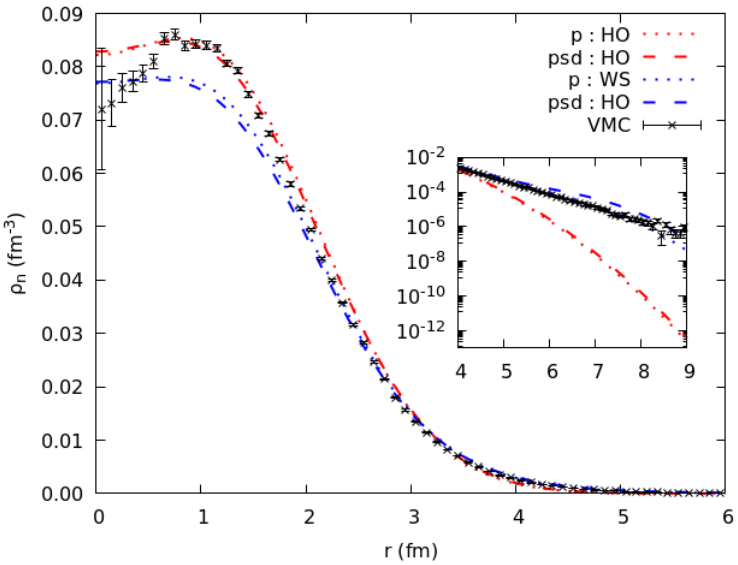

Figure 13: Neutron density profile of ^{10}Be. Same as Figure 11, with the addition of shell model calculations in the *p*- and *psd*-shell configuration spaces using WS radial wavefunctions (blue dotted and dashed lines, respectively).

In Figures 12 and 13 we can see that, as well as with the HO case, the WS densities differ from the VMC calculations at small r, but are in reasonable agreement for intermediate values of r. However, in Figures we can distinguish how the asymptotic behaviour of the WS wavefunctions is in a good agreement with the VMC data, in contrast to the HO case. This makes the Woods-Saxon potential a more realistic potential to use.

We can expect a overall similar behaviour for $A = 12$, but it might be useful to check if it also holds up for the heavier cases like $A = 48$. Thus, we present the oscillator amplitudes (Tables 9 and 10) and nucleon density profiles (Figures 14 and 15) of ^{48}Ca. Figures 14 and 15 show a similar asymptotic behaviour when comparing HO and WS wavefunctions for $A = 48$.

nlj	ε_{nlj}	$\nu = 0$	$\nu = 1$	$\nu = 2$	$\nu = 3$	$\nu = 4$	$\nu = 5$
$0s_{1/2}$	-25.423	0.989	-0.143	-0.029	-0.010	0.005	0.003
$0p_{3/2}$	-17.753	0.994	-0.107	-0.025	-0.024	0.003	0.004
$0p_{1/2}$	-15.709	0.997	-0.066	-0.014	-0.027	-0.001	0.001
$0d_{5/2}$	-9.410	0.996	-0.079	-0.002	-0.039	0.002	0.001
$1s_{1/2}$	-5.961	0.138	0.977	-0.146	0.036	-0.061	0.010
$0d_{3/2}$	-5.237	0.997	-0.045	0.036	-0.044	0.003	-0.006

Table 9: Woods-Saxon energies ε_{nlj} and oscillator amplitudes $A_\nu^{(nlj)}$ for proton single-particle states in ^{48}Ca, calculated using the WS parameters from Eqs. (66)-(68).

nlj	ε_{nlj}	$\nu = 0$	$\nu = 1$	$\nu = 2$	$\nu = 3$	$\nu = 4$	$\nu = 5$
$0s_{1/2}$	-35.021	0.995	-0.098	-0.035	-0.011	0.003	0.003
$0p_{3/2}$	-26.724	0.998	-0.053	-0.032	-0.023	0.000	0.004
$0p_{1/2}$	-24.711	0.999	-0.012	-0.019	-0.024	-0.004	0.001
$0d_{5/2}$	-17.768	0.999	-0.016	-0.012	-0.033	-0.004	0.001
$1s_{1/2}$	-14.269	0.096	0.993	-0.051	0.011	-0.046	-0.001
$0d_{3/2}$	-13.566	0.999	0.027	0.022	-0.032	-0.005	-0.005
$0f_{7/2}$	-8.421	0.999	-0.003	0.027	-0.046	-0.002	-0.005
$1p_{3/2}$	-5.043	0.050	0.981	-0.135	0.094	-0.086	0.014
$0f_{5/2}$	-1.938	0.992	-0.026	0.107	-0.061	0.018	-0.019
$1p_{1/2}$	-3.084	0.012	0.972	-0.159	0.140	-0.099	0.022

Table 10: Woods-Saxon energies ε_{nlj} and oscillator amplitudes $A_\nu^{(nlj)}$ for neutron single-particle states in ^{48}Ca, calculated using the WS parameters from Eqs. (66)-(68).

We have included the Woods-Saxon energies and oscillator amplitudes of all the other cases we will be treating in this chapter in Appendix D (Tables 15-24). Note that this only refers to neutrons of the parent nuclei and protons of the daughter nuclei, as we are interested in the study of double-beta decay.

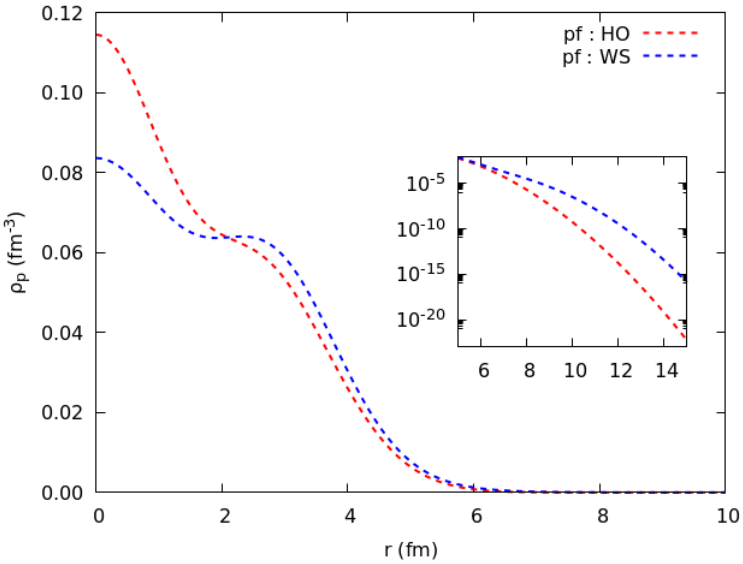

Figure 14: Proton density profile of ^{48}Ca. The dashed red (blue) line corresponds to shell model calculations in the pf-shell configuration space using HO (WS) radial wavefunctions. The asymptotic behaviour of the density profile has been included.

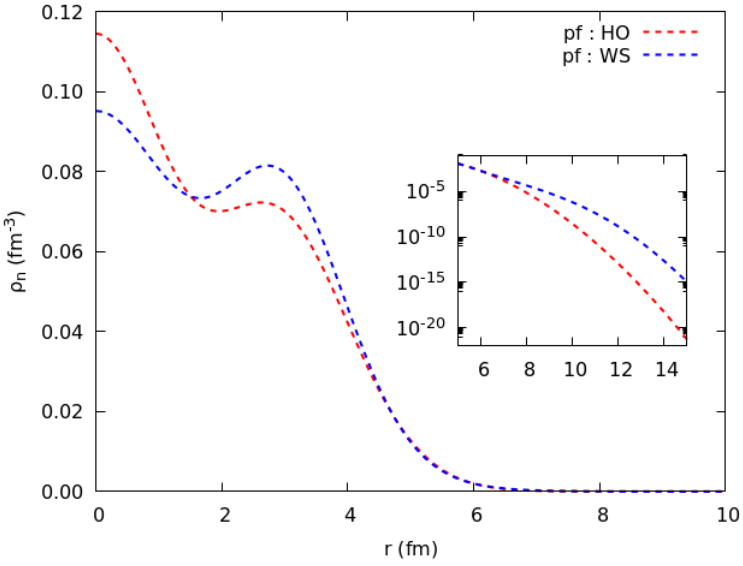

Figure 15: Neutron density profile of ^{48}Ca. The dashed red (blue) line corresponds to shell model calculations in the pf-shell configuration space using HO (WS) radial wavefunctions. The asymptotic behaviour of the density profile has been included.

3.2.1 Separation energies

Up until now, we have followed the usual parametrization for the Woods-Saxon potential (Eqs. (66)-(68)). However, Wang et al. [27] introduced a different parametrization: they took the p-shell proton and neutron asymptotic wavefunction behaviour to be determined by the corresponding separation energies, while the unbound sd-shell particles are assumed to be bound by ~ 0.05 MeV.

HO wavefunctions decay rapidly at great distances, with an asymptotic form $e^{-(r/b)^2}$. WS wavefunctions, on the other hand, decay less dramatically, like e^{-kr} [36], with

$$k = \frac{\sqrt{2\mu B_s}}{\hbar}, \tag{76}$$

where μ is the reduced mass of the last nucleon and the resulting nucleus and

$$B_s = B(^{\mathrm{A}}\mathrm{X}) - B(^{\mathrm{A-1}}\mathrm{Y}) \tag{77}$$

is the separation energy of the last nucleon. We calculate B_s from the binding energies of the original ($^{\mathrm{A}}$X) and the resulting nucleus ($^{\mathrm{A-1}}$Y), taken from [20, 21].
Thus, using Equation (76), we can find the k parameter for each case and fit the asymptotic behaviour of our p-shell WS wavefunctions by modifying the V_0 parameter of the WS potential. From now on, the usual parametrization will be referred as Suhonen (S) parametrization, while the new one based on the separation energies will be called Wang (W) parametrization.

$^{\mathrm{A}}$X	N	B_s (MeV)	k (fm^{-1})	$V_{0,S}$ (MeV)	k_S (fm^{-1})	$V_{0,W}$ (MeV)	k_W (fm^{-1})
^{10}Be	n	6.812	0.543	44.4	0.822	33.7	0.639
^{10}C	p	4.007	0.417	44.4	0.782	42.3	0.748
^{12}Be	n	3.171	0.374	40.0	0.647	29.7	0.574
^{12}C	p	15.957	0.839	51.0	0.909	46.2	0.839

Table 11: Suhonen and Wang WS parametrizations for the nuclei involved in the double-beta decays ^{10}Be $\rightarrow$ ^{10}C and ^{12}Be $\rightarrow$ ^{12}C.

As we can see in Table 11 above, it is not possible to exactly fit k_W to k for most of the cases. This is because, as V_0 decreases, the single-particle states become more unbound. As such, we fitted k_W as close as we could to k while keeping all the single-particle states of the p-shell bound by ~ 0.05 MeV. However, for the case of the ^{12}C protons, we have been able to fit $k = k_W$ since none of the p-shell states became unbound.

We extended this parametrization to the double-beta decay of heavier nuclei like ^{48}Ca. In this case, we fitted the asymptotic behaviour of the wavefunction up to the pf-shell, while making sure that all single-particle states are bound by ~ 0.05 MeV. Here, each orbital of the pf-shell has its own V_0 (which is what we did for the sd-shell in the previous case),

which is the reason why we did not present any single V_0 values in Table 12 as we did in Table 11.

^{A}X	N	B_s (MeV)	k (fm^{-1})	k_S (fm^{-1})	k_W (fm^{-1})
^{48}Ca	n	9.952	0.685	0.900	0.685
^{48}Ti	p	11.878	0.749	0.993	0.832

Table 12: Suhonen and Wang WS parametrizations for the nuclei involved in the double-beta decay $^{48}\text{Ca} \to {}^{48}\text{Ti}$.

The Woods-Saxon energies and oscillator amplitudes obtained through Wang's parametrization have been included in Appendix D.

3.3 Transition densities

Prior to begin studying the nuclear matrix elements, we will first compare the wavefunction transition densities, defined as

$$C(r) = \langle f | \sum_{a<b} \delta(r - r_{ab}) \tau_a^+ \tau_b^+ | i \rangle. \tag{78}$$

Shell model calculations generally use HO radial wavefunctions, since the HO basis provides the advantage of a simple well-defined method of separating into center-of-mass and relative coordinates via a Talmi-Moshinsky transformation [37, 38].

For that reason, we built a new option which, introducing the oscillator amplitudes we obtained in section 3.2, finally allows us to obtain results with WS wavefunctions. To do this, we also generalized the Talmi-Moshinsky transformation from HO wavefunctions to WS wavefunctions in HO basis.

Following Equation (72), we express the two-body WS wavefunction in HO basis as

$$|n_1 l_1 j_1 t_1, n_2 l_2 j_2 t_2; J\rangle_{\text{WS}} = \sum_{\nu_1 \nu_2} A_{\nu_1}^{(n_1 l_1 j_1)} A_{\nu_2}^{(n_2 l_2 j_2)} |\nu_1 l_1 j_1 t_1, \nu_2 l_2 j_2 t_2; J\rangle_{\text{HO}} \tag{79}$$

so we can expand the corresponding Talmi-Moshinsky transformation as

$$\begin{aligned} &{}_{\text{WS}}\langle n_1' l_1' j_1' p, n_2' l_2' j_2' p; J | O_\alpha | n_1 l_1 j_1 n, n_2 l_2 j_2 n; J\rangle_{\text{WS}} = \\ &= \sum_{\nu_1 \nu_2 \nu_1' \nu_2'} A'_{\nu_1'}{}^{(n_1' l_1' j_1')} A'_{\nu_2'}{}^{(n_2' l_2' j_2')} A_{\nu_1}^{(n_1 l_1 j_1)} A_{\nu_2}^{(n_2 l_2 j_2)} {}_{\text{HO}}\langle \nu_1' l_1' j_1' p, \nu_2' l_2' j_2' p; J | O_\alpha | \nu_1 l_1 j_1 n, \nu_2 l_2 j_2 n; J\rangle_{\text{HO}} \end{aligned} \tag{80}$$

where $O_\alpha = \tau_1^+ \tau_2^+ \, S_\alpha \, H_\alpha(r) \, \tilde{H}_\alpha(R)$, with $r = |\mathbf{r}_1 - \mathbf{r}_2|$ the relative radial coordinate (distance between decaying neutrons) and $R = |\mathbf{r}_1 + \mathbf{r}_2|$ the center-of-mass radial coordinate. The full expansion of this transformation can be found in Appendix E.

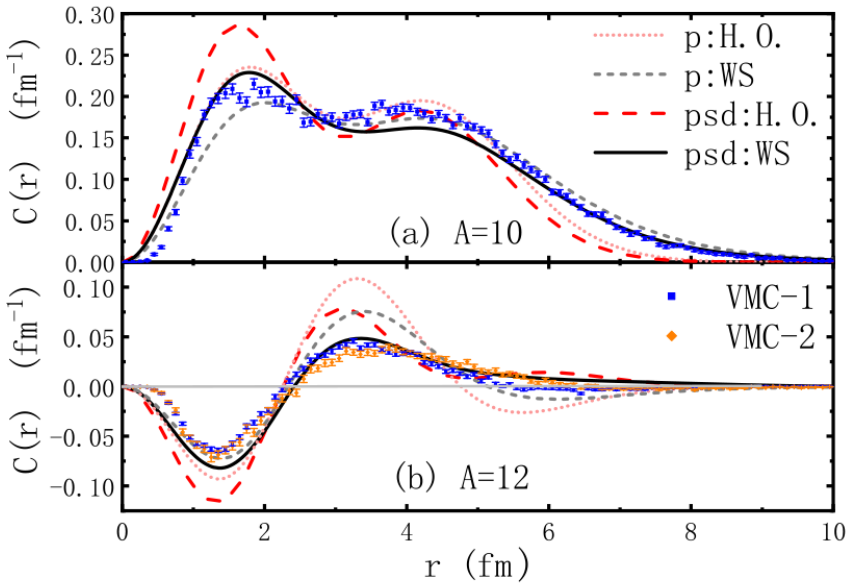

Figure 16: The normalization densities $C(r)$, for (a) $A = 10$, and (b) $A = 12$. The $N = 1$ model space (p-shell only) and extended model space of *psd* shell model calculation results are shown. The different choices of radial wavefunctions, HO, and WS, are also shown. VMC results with shell-model-like wavefunctions are labeled as "VMC-1", and those with cluster-like wave functions are labeled as "VMC-2". Taken from [27].

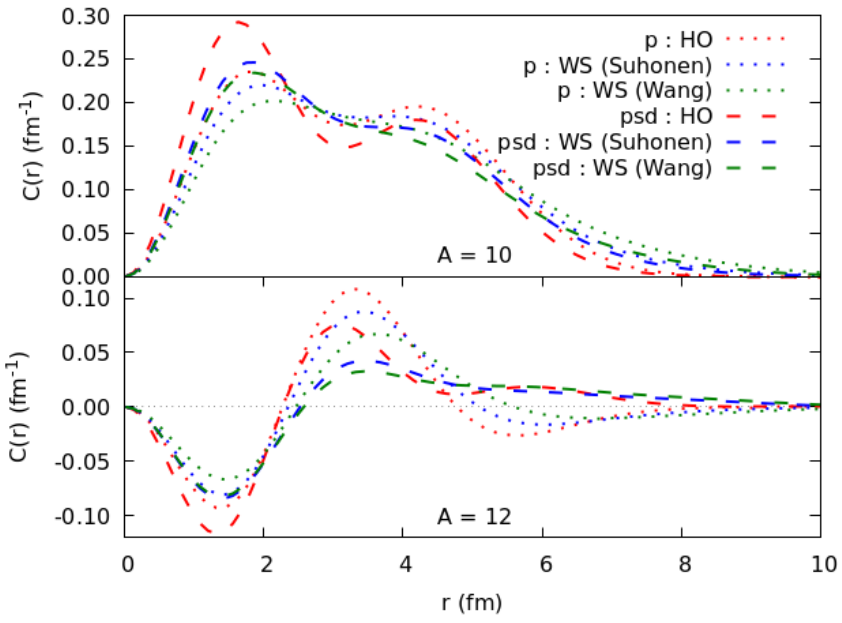

Figure 17: Our rendition of the normalization densities $C(r)$ for $A = 10$ and $A = 12$. The green dotted and dashed lines would correspond to our version of the WS data in Figure 16, using the same parametrization as [27]. The blue lines would correspond to the usual WS parametrization.

Figure 16 shows the transition density of ^{10,12}Be $\rightarrow$ ^{10,12}C calculated with the shell model in the *p*- and *psd*-shell configurations spaces, compared to VMC calculations as obtained in reference [27]. On the other hand, Figure 17 aims to reproduce the shell model results of Figure 16 by using the Suhonen and Wang Woods-Saxon parametrization sets described in subsection 3.2.1.

Figure 16 shows that the WS wavefunctions provide a better description at large distances, as we previously checked in section 3.2. The normalization of $C(r)$ for the $A = 10$ transition is $\int_0^\infty C(r)\,dr = 1$ due to the parent and daughter nuclei being mirror nuclei (^{10}Be and ^{10}C), while being $\int_0^\infty C(r)\,dr = 0$ for the $A = 12$ transition.
However, the normalizations we obtained in our first WS results ranged around 0.90-0.98 for $A = 10$ and 10^{-3}-10^{-2} for $A = 12$, making us realize our calculation wasn't correct. This made us acknowledge the isospin symmetry breaking introduced by the oscillator amplitudes $A_\nu^{(nlj)}$. Accordingly, we upgraded our code in order to distinguish between protons and neutrons, and modified the effective hamiltonian files to substitute the general nucleon-nucleon interactions for proton-proton, neutron-neutron and proton-neutron interactions. This way, the normalizations correctly converged to 1 for $A = 10$ and 0 for $A = 12$.

An important thing to note is that, for $A = 12$, there is a node around $r \sim 5\,\text{fm}$ that appears for *p*-shell calculations and does not for *psd* and VMC, highlighting the impact that different model spaces can have for the calculation.

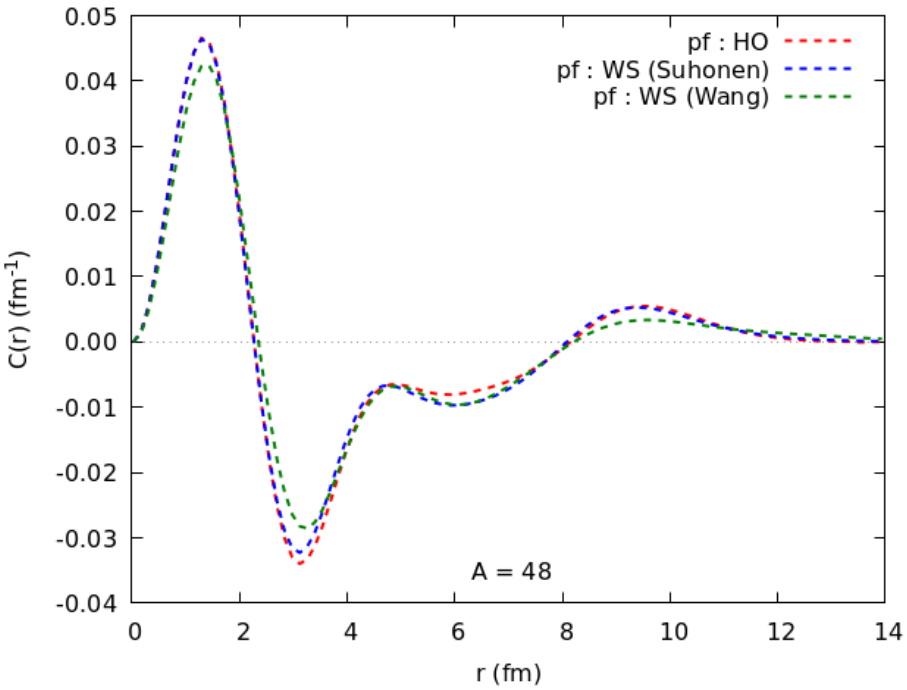

Figure 18: Normalization density $C(r)$ for $A = 48$. The color code is the same as Figures 16 and 17, but for the pf-shell instead.

Even though our results are qualitatively similar to Wang et al.'s, there exist a couple differences regarding our Wang WS parametrization: the second peak for $A = 10$ appears to be smoothed out, and the positive peak of the p-shell calculation for $A = 12$ seems to be slightly lower. We have tried to pinpoint the source of this difference without success.

We also calculated the normalization density for $A = 48$ using the WS parametrizations described in subsection 3.2.1. Figure 18 indicates that, although the differences are not as obvious as for lighter nuclei, there still exist non-negligible discrepancies between HO and WS wavefunctions, especially for Wang's parametrization.

3.4 Radial distribution of the NME components

Just as we calculated the normalization densities in the previous section, we can also represent the radial NME distributions $C_{GT}(r)$, $C_F(r)$ and $C_T(r)$, which fulfill the property

$$M^{0\nu}_{GT} = \int_0^\infty C_{GT}(r)\, dr\,, \qquad M^{0\nu}_{F} = \int_0^\infty C_{F}(r)\, dr\,, \qquad M^{0\nu}_{T} = \int_0^\infty C_{T}(r)\, dr\,, \tag{81}$$

where $M^{0\nu}_{GT}$, $M^{0\nu}_{F}$ and $M^{0\nu}_{T}$ are explained in section 1.1 and defined in Equations (29)-(31).

As we have seen in the previous section, the extended psd-shell configuration space provides a better description than p-shell for light ($A = 10, 12$) nuclei. Thus, we have represented the radial distributions from Equation (81) in Figures 19-24 and the integrated matrix elements in Tables 13 and 14 working in the psd-shell for $A = 10, 12$ and the pf-shell for $A = 48$, using HO and WS radial wavefunctions.

Figures 19 through 22 show a lower first peak in the radial distribution of the NMEs for the WS results in light nuclei (except for the tensor component in the $A = 10$ case, which presents a higher peak for WS calculations). As we can see in Table 13, this results in lower values of the total NME $M^{0\nu}$, which implies corrections ranging between $\sim$ 13%-16% for $A = 10$ and $\sim$ 7%-15% for $A = 12$, depending on the chosen WS parametrization.

On the other hand, for heavier nuclei ($A = 48$), Figures 23 and 24 show that the Suhonen WS parametrization gives off radial distributions very similar to the HO case, while the Wang parametrization presents slightly more prominent differences to both of them. Table 14 shows us this true for $M^{0\nu}_{F}$ and $M^{0\nu}_{T}$, presenting differences below 1% between Suhonen WS and HO results. However, even while having a visually similar profile, this difference goes up to more than 4% for $M^{0\nu}_{G}T$. This is due to different cancellations happening beyond the first peak: as we can see in Figure 23, in the second peak HO results present more negative values than Suhonen WS's. If we zoom in at the tail of the profile ($r > 4$fm), we can distinguish how $C_{GT}(r)$ still presents a negative value until $r \sim 7$ fm for the HO results, while Suhonen WS's $C_{GT}(r)$ stays positive beyond $r \sim 4.5$ fm. Both of this differences add up, resulting in a more important cancellation for the HO case, and finally resulting in a $\sim$ 4.5% difference for the total NME $M^{0\nu}$. Wang's parametrization, on the other hand, presents roughly half that difference, at $\sim$ 2.2%.

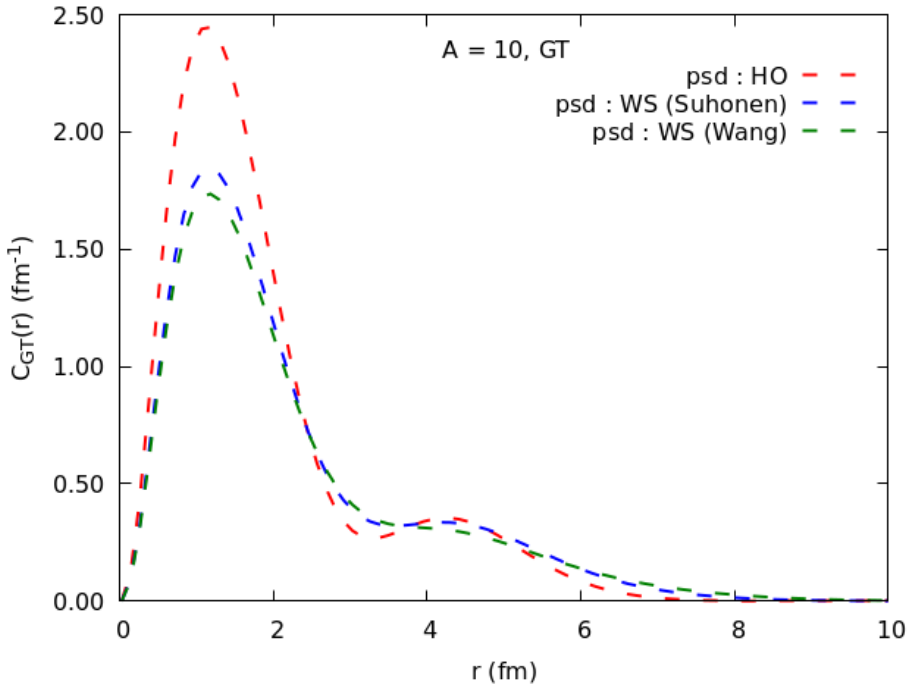

Figure 19: Radial distribution $C_{GT}(r)$ (Equation (77)) for $A = 10$, calculated in the *psd*-shell configuration space and using different radial wavefunctions.

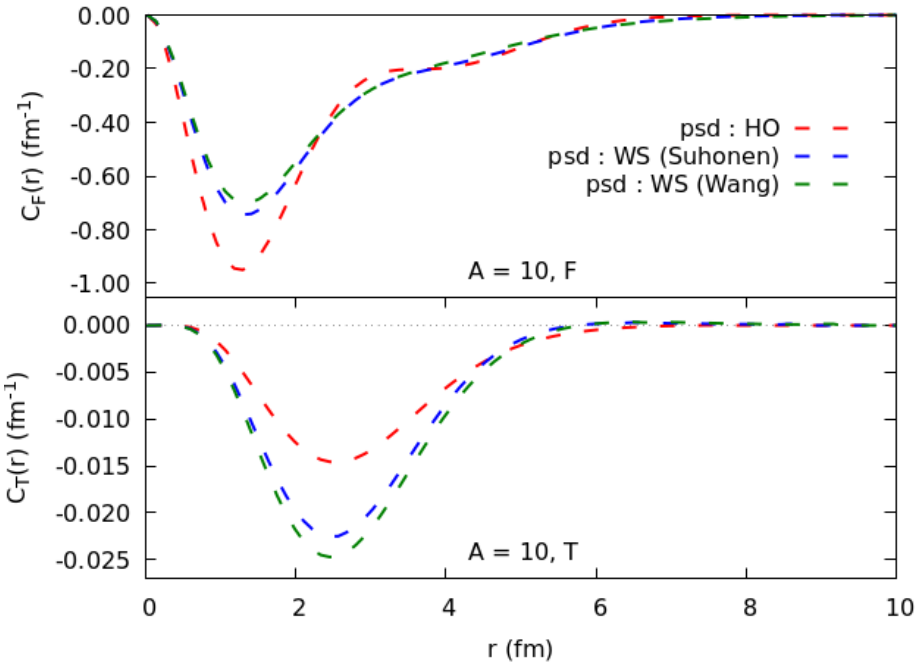

Figure 20: Radial distributions $C_F(r)$ and $C_T(r)$ (Equation (77)) for $A = 10$, calculated in the *psd*-shell configuration space and using different radial wavefunctions.

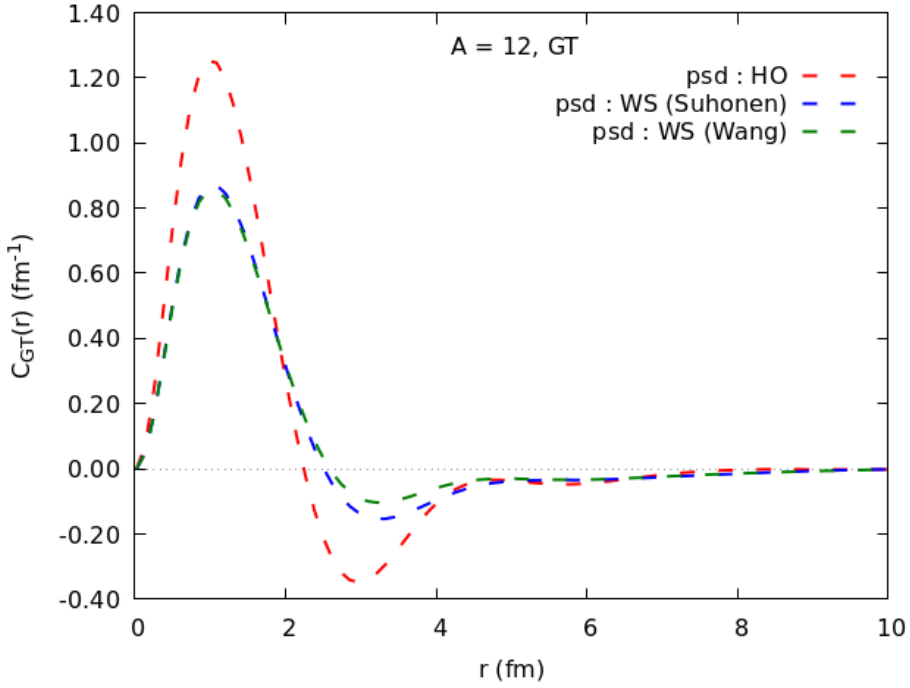

Figure 21: Radial distribution $C_{GT}(r)$ (Equation (77)) for $A = 12$, calculated in the *psd*-shell configuration space and using different radial wavefunctions.

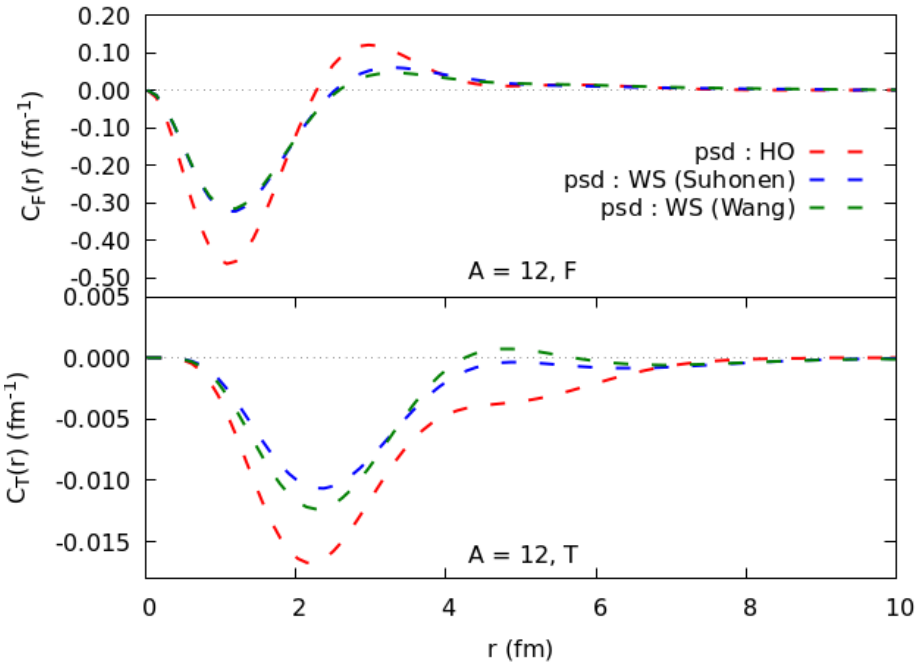

Figure 22: Radial distributions $C_F(r)$ and $C_T(r)$ (Equation (77)) for $A = 10$, calculated in the *psd*-shell configuration space and using different radial wavefunctions.

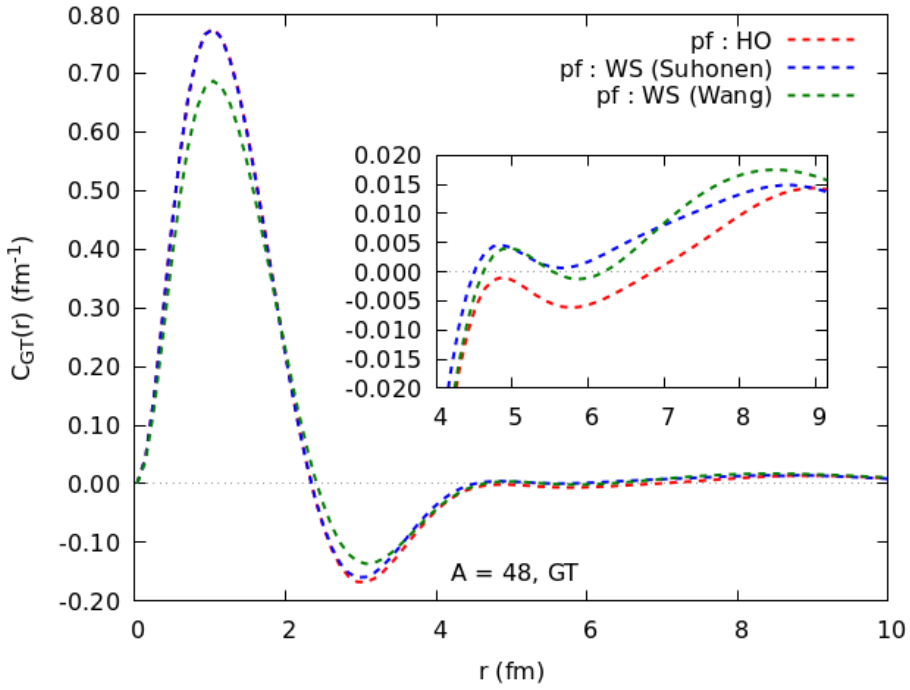

Figure 23: Radial distribution $C_{GT}(r)$ (Equation (77)) for $A = 48$, calculated in the pf-shell configuration space and using different radial wavefunctions. The tail is shown in detail to observe the different cancellations.

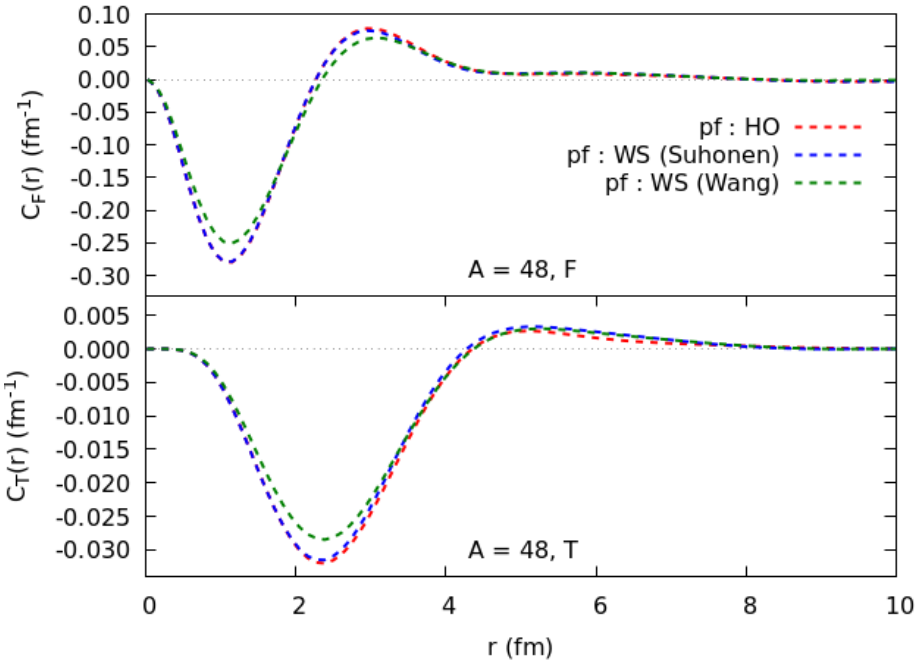

Figure 24: Radial distributions $C_F(r)$ and $C_T(r)$ (Equation (77)) for $A = 10$, calculated in the pf-shell configuration space and using different radial wavefunctions.

Regarding the introduced corrections, Table 13 shows that WS radial wavefunctions reduce the total NME $M^{0\nu}$ for $A = 10, 12$, while Table 14 shows that they may either reduce or enhance $M^{0\nu}$ for $A = 48$, depending on the chosen parametrization.

In the end, the more realistic WS radial wavefunctions introduce a correction to the $0\nu\beta\beta$ decay rate of up to $\sim 30\%$ for light nuclei (like ^{10}Be and ^{12}Be) and $\sim 9\%$ for the decay of a heavier nuclei like ^{48}Ca when compared to the decay rate obtained with HO radial wavefunctions.

	$^{10}\text{Be} \rightarrow {}^{10}\text{C}$				$^{12}\text{Be} \rightarrow {}^{12}\text{C}$			
	$M^{0\nu}_{GT}$	$M^{0\nu}_{F}$	$M^{0\nu}_{T}$	$M^{0\nu}$	$M^{0\nu}_{GT}$	$M^{0\nu}_{F}$	$M^{0\nu}_{T}$	$M^{0\nu}$
psd : HO	4.90	-2.11	-0.038	6.16	1.03	-0.390	-0.042	1.22
psd : WS (S)	4.26	-1.90	-0.053	5.39	0.867	-0.315	-0.024	1.04
psd : WS (W)	4.11	-1.83	-0.059	5.18	0.951	-0.321	-0.024	1.13

Table 13: $M^{0\nu}$ and its Gamow-Teller, Fermi and tensor components for the double-beta decay ^{10}Be $\rightarrow$ ^{10}C ($A = 10$) and ^{12}Be $\rightarrow$ ^{12}C ($A = 12$), calculated in the *psd*-shell configuration space and using different radial wavefunctions.

	$^{48}\text{Ca} \rightarrow {}^{48}\text{Ti}$			
	$M^{0\nu}_{GT}$	$M^{0\nu}_{F}$	$M^{0\nu}_{T}$	$M^{0\nu}$
pf : HO	0.845	-0.228	-0.058	0.929
pf : WS (S)	0.882	-0.230	-0.054	0.970
pf : WS (W)	0.825	-0.217	-0.050	0.909

Table 14: $M^{0\nu}$ and its Gamow-Teller, Fermi and tensor components for the double-beta decays ^{48}Ca $\rightarrow$ ^{48}Ti ($A = 48$), calculated in the pf-shell configuration space and using different radial wavefunctions.

4 Summary and conclusions

The observation of a neutrinoless double-beta ($0\nu\beta\beta$) decay would imply that neutrinos are Majorana fermions. $0\nu\beta\beta$ decay would violate the conservation of the lepton number and, potentially, of the baryon-lepton number too, opening a doorway to the Physics beyond the Standard Model potentially shedding some light to the matter-antimatter asymmetry in the universe.

The half-life of such a process depends on the nuclear matrix element $M^{0\nu}$ and a combination of the neutrino masses, $m_{\beta\beta}$. Thus, once it is detected, obtaining accurate values of the NME would be vital to obtain information about the absolute scale of the neutrino masses and its ordering.

In the first part of this work, we reviewed the contribution to the $0\nu\beta\beta$ decay amplitude from low-momentum neutrinos (known as the ultrasoft regime [9]), which is usually neglected. Using the nuclear shell model, we numerically calculated this contribution for the first time and the correction it represents for the $0\nu\beta\beta$ decay rate of ^{48}Ca ($\sim 2.4\%$) and ^{136}Xe ($\sim 8.6\%$), which agrees with the order of magnitude estimated in reference [9]. We analyzed the dependence of this contribution with using different effective interactions for ^{136}Xe and obtained similar results, with corrections to the $0\nu\beta\beta$ decay rate ranging from $\sim 5.2\%$ to $\sim 8.6\%$.

We discussed the case of computationally demanding calculations like the $0\nu\beta\beta$ decay of ^{128}Te and ^{130}Te by studying similar isotopes in order to get an approximated idea of its results. Our findings suggest a impact comparable to that of the $0\nu\beta\beta$ decay of ^{136}Xe.

Compared to the $2\nu\beta\beta$ amplitude, $M^{2\nu}_{GT}$ is more sensitive to contributions from low energy intermediate states ($E_n - E_i < 5\,\mathrm{MeV}$) while $M^{0\nu}_{\mathrm{usoft}}$ is more sensitive to contributions in the 5 - 10 MeV region.

In the second part of this work, we studied the impact of realistic radial wavefunctions (like the ones that arise from the phenomenological Woods-Saxon potential) on calculations of NMEs when compared to the typically used harmonic oscillator wavefunctions.

First, we compared nucleon densities calculated with the harmonic oscillator radial wavefunctions and compared it to results obtained through the more sophisticated variational Monte Carlo (VMC) method [35]. The HO radial wavefunctions do not provide a good asymptotic description, highlighting the need for a better, more realistic potential. Thus, we implemented Woods-Saxon radial wavefunctions into the shell model framework described in a HO basis. In contrast to the HO, the WS radial wavefunctions present the correct asymptotic behaviour when compared to the VMC results.

Using the nuclear shell model, we built an option to calculate transition densities using WS radial wavefunctions. We calculated these transition densities for the $0\nu\beta\beta$ decay of

light nuclei ($A = 10$ and $A = 12$) with HO and WS radial wavefunctions and using two different valence spaces (the p-shell and the extended psd-shell) and compared them to the ones from reference [27], finding an overall similar structure with small discrepancies. For the first time, we extended this study to the $0\nu\beta\beta$ decay of heavier nuclei ($A = 48$) in the pf-shell valence space. Our results show smaller yet non-negligible differences between calculations using HO and WS wavefunctions.

Lastly, we calculated the radial distribution of the Gamow-Teller, Fermi and tensor components of the $M^{0\nu}$ nuclear matrix element for light ($A = 10, 12$) and heavy ($A = 48$) nuclei. As expected from the study of the transition densities, we obtained non-negligible corrections to the NME when using different radial wavefunctions. In particular, we obtained corrections to $M^{0\nu}$ ranging between $\sim 10\%$ and $\sim 16\%$ for the $0\nu\beta\beta$ decay of ^{10}Be and ^{12}Be. For the first time, we also carried out calculations for the more relevant decay of the ^{48}Ca nuclei (being the lightest experimentally observed nuclei to undergo $0\nu\beta\beta$ decay), finding a correction to $M^{0\nu}$ ranging between $\sim 2.2\%$ and $\sim 4.5\%$.

Overall, our study suggest that usually neglected corrections to the $0\nu\beta\beta$ NME can represent a contribution of up to $\sim 5\%$. Combined, the two aspects that have been adressed in this work can represent an enhancement to the NME of $\sim 10\%$, leading to a reduction of $\sim 20\%$ of the $0\nu\beta\beta$ decay half-life. Therefore, these contributions can be relevant in order to extract information of interest from $0\nu\beta\beta$ decay experiments.

A Appendix A: Correction to the electron energies

In section 2.3, we made the approximation $E_1 = E_2 \simeq Q_{\beta\beta}/2$. The correction to this approximation is

$$E_1 = \frac{Q_{\beta\beta}}{2} - \delta\,, \quad E_2 = \frac{Q_{\beta\beta}}{2} + \delta\,, \tag{82}$$

where $-Q_{\beta\beta}/2 \leq \delta \leq Q_{\beta\beta}/2$. Substituting these energies into the expression of $M^{0\nu}_{\text{usoft}}$ and performing a series expansion, we find

$$\begin{aligned} M^{0\nu}_{\text{usoft}}(n) = \frac{R}{2\pi}\sum_n \langle f|\boldsymbol{\sigma}\tau^+|n\rangle\langle n|\boldsymbol{\sigma}\tau^+|i\rangle \times \Bigg[2\left(\frac{Q_{\beta\beta}}{2} + E_n - E_i\right) \\ \times \left(\ln\frac{m_\pi}{2\left(\frac{Q_{\beta\beta}}{2} + E_n - E_i\right)} + 1\right) + \frac{\delta^2}{\frac{Q_{\beta\beta}}{2} + E_n - E_i} + \mathcal{O}(\delta^4)\Bigg] \end{aligned} \tag{83}$$

where the first term of the sum is the one that we used in the calculations, while the second term is the associated correction.

For a typical intermediate state with $E_n - E_i \sim \mathcal{O}(5 - 10\,\text{MeV})$, and considering the maximum possible deviation from the approximation ($|\delta| = Q_{\beta\beta}/2$), this correction can amount up to $\sim 7\%$ for the $0\nu\beta\beta$ decay of ^{48}Ca and $\sim 3\%$ for ^{136}Xe. Thus, $E_{1,2} \simeq Q_{\beta\beta}/2$ is a good approximation to calculate $M^{0\nu}_{\text{usoft}}$.

B Appendix B: Convergence of $S(n_{\max})$ and $M^{0\nu}_{\text{usoft}}$

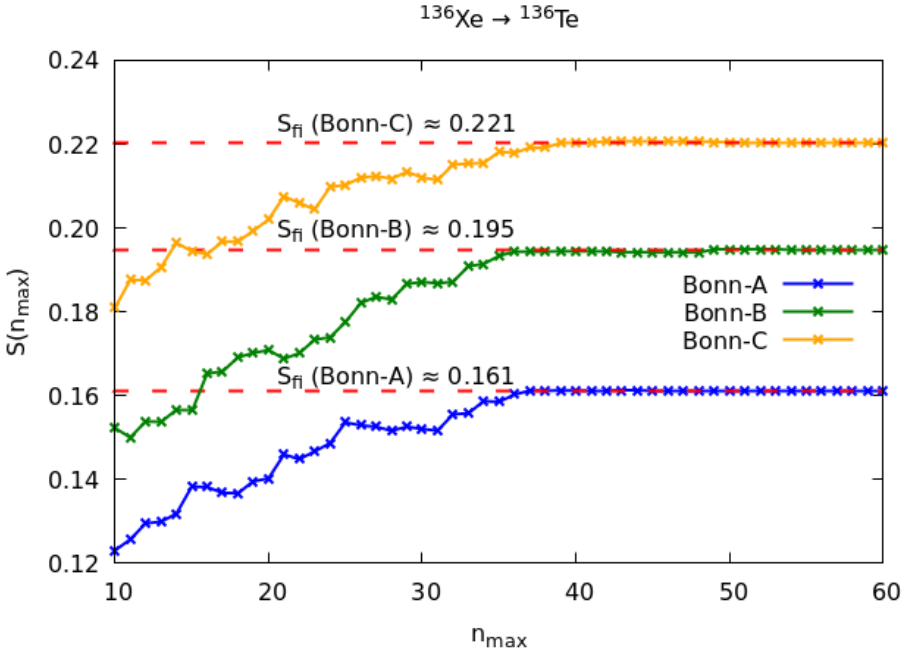

Figure 25: $S(n_{\max})$ for the double-beta decay of ^{136}Xe, using different Bonn interactions.

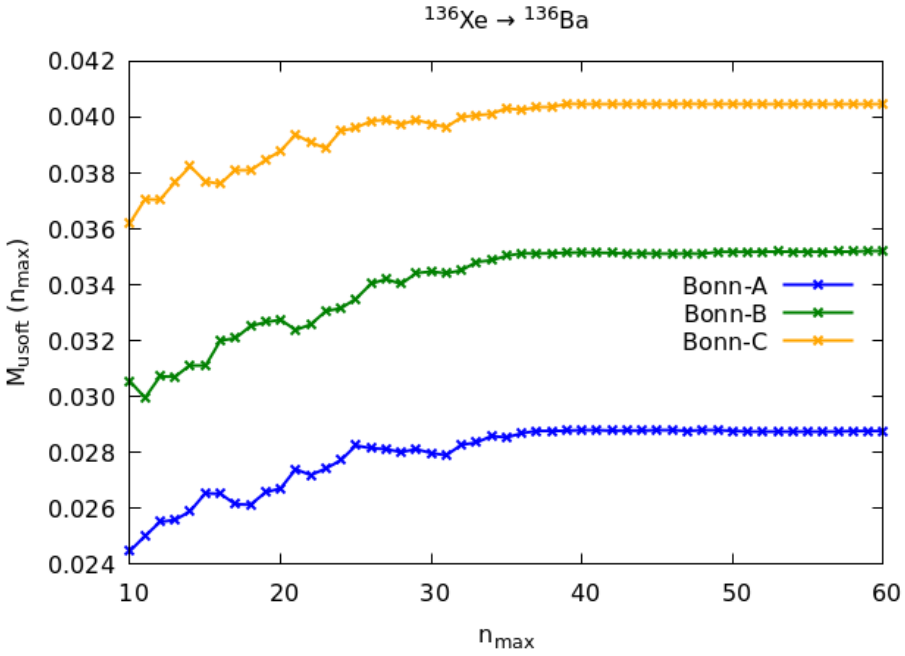

Figure 26: Matrix element $M^{0\nu}_{\text{usoft}}$ with respect to the number 1^+ of intermediate states $n_{\max}$ for the double-beta decay of ^{136}Xe, using different Bonn interactions.

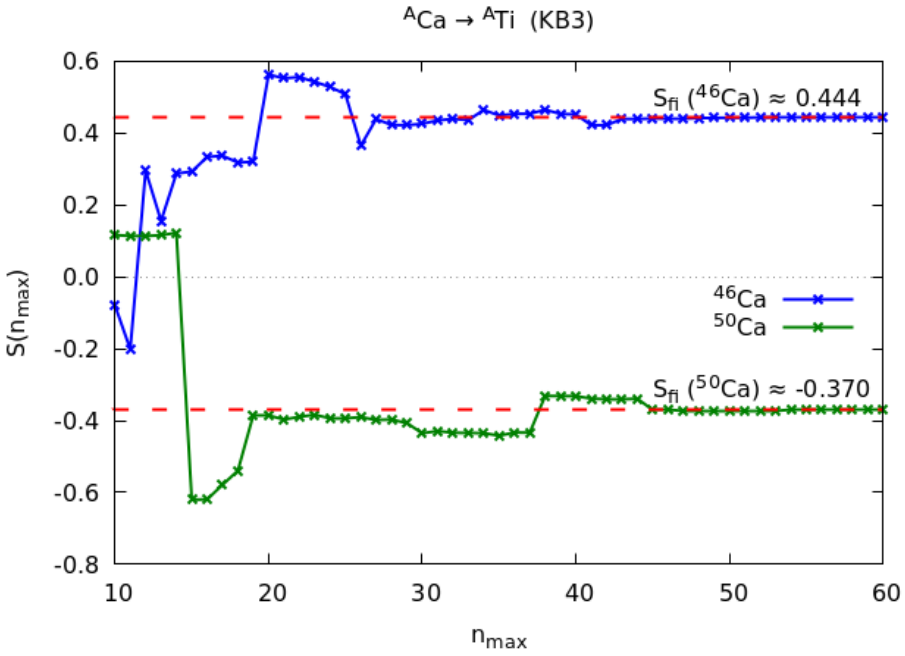

Figure 27: $S(n_{\max})$ for the double-beta decay of ^{46}Ca and ^{50}Ca, using the KB3 interaction.

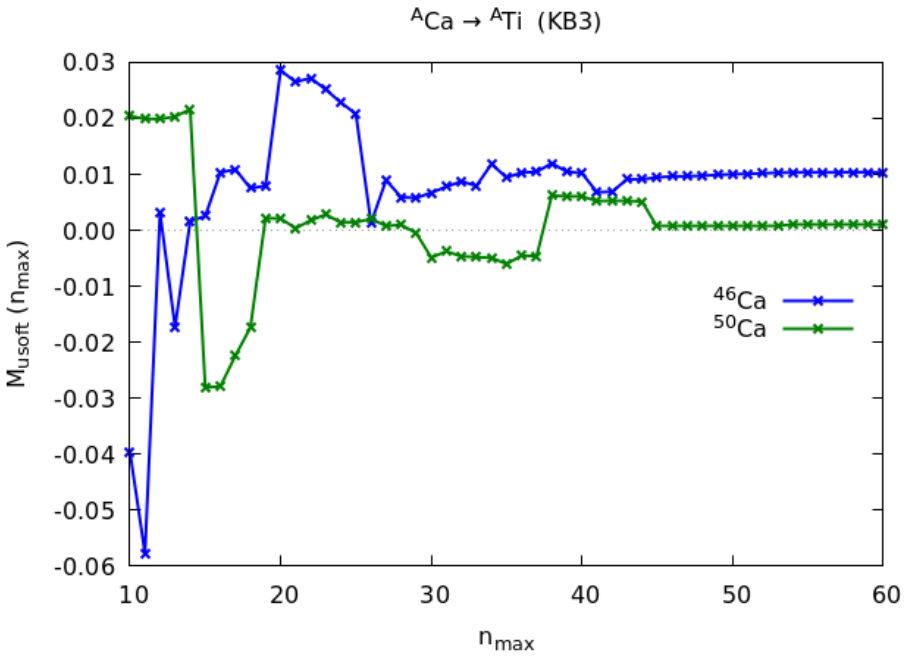

Figure 28: Matrix element $M^{0\nu}_{\text{usoft}}$ with respect to the number 1^+ of intermediate states $n_{\max}$ for the double-beta decay of ^{46}Ca and ^{50}Ca, using the KB3 interaction.

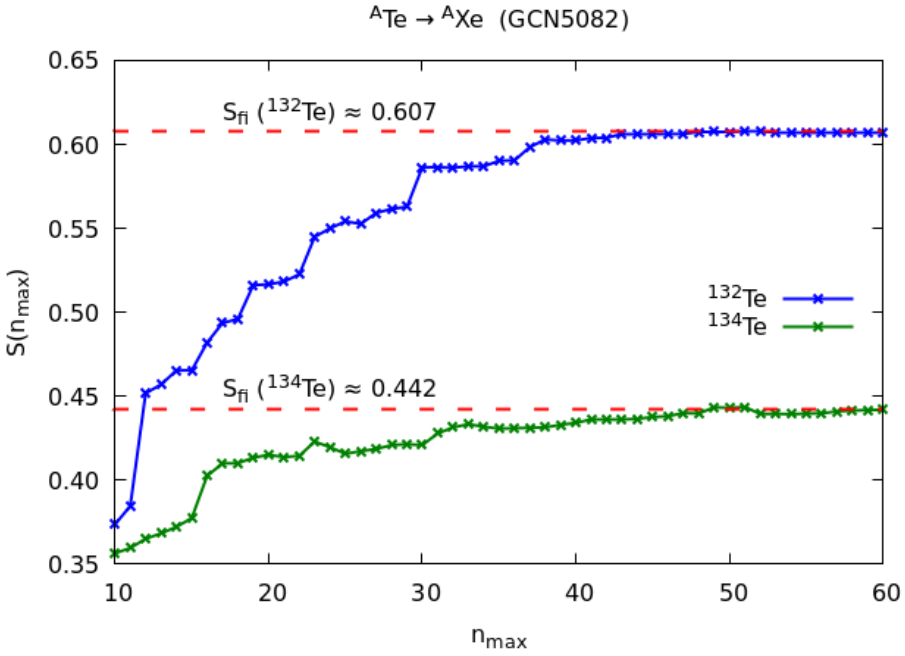

Figure 29: $S(n_{\max})$ for the double-beta decay of ^{132}Te and ^{134}Te, using the GCN5082 interaction.

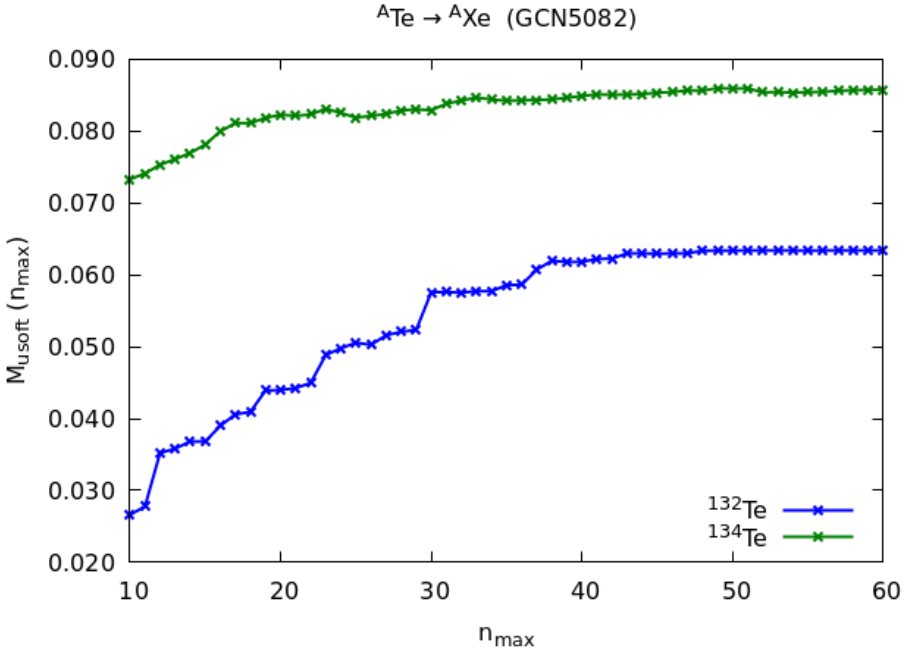

Figure 30: Matrix element $M^{0\nu}_{\text{usoft}}$ with respect to the number 1^+ of intermediate states $n_{\max}$ for the double-beta decay of ^{132}Te and ^{134}Te, using the GCN5082 interaction.

C Appendix C: Associated Laguerre polynomials

Back in Equation (61), we defined the harmonic oscillator radial wavefunction $g_{nl}(r)$ using the associated Laguerre polynomials $L_n^{(l+\frac{1}{2})}(x)$ [30].

The first three associated Laguerre polynomials are

$$L_0^{(l+\frac{1}{2})} = 1\,, \tag{84}$$

$$L_1^{(l+\frac{1}{2})} = l - x + \frac{3}{2}\,, \tag{85}$$

$$L_2^{(l+\frac{1}{2})} = \frac{1}{2}\left[\left(l+\frac{3}{2}\right)\left(l+\frac{5}{2}\right) - 2\left(l+\frac{5}{2}\right)x + x^2\right]\,, \tag{86}$$

while further polynomials can be obtained through the recursion relation

$$L_n^{(l+\frac{1}{2})} = L_n^{(l+\frac{3}{2})} - L_{n-1}^{(l+\frac{3}{2})}. \tag{87}$$

Instead of directly using these polynomials, numerical values for $g_{nl}(r)$ can be obtained through the auxiliary functions $v_{nl}(r)$ [39], defined by

$$g_{nl}(r) = \sqrt{\frac{2^{-n+l+2}(2n+2l+1)!!}{b^3\sqrt{\pi}n![(2l+1)!!]^2}}\left(\frac{r}{b}\right)^l e^{-r^2/2b^2} v_{nl}\left(\frac{r^2}{b^2}\right), \tag{88}$$

and then using the recursion relations

$$v_{n,l-1}(x) = v_{n-1,l-1}(x) - \frac{2x v_{n-1,l}(x)}{2l+1}\,, \tag{89}$$

$$v_{nl}(x) = \frac{(2l+1)v_{n,l-1}(x) + 2n v_{n-1,l}(x)}{2n+2l+1}\,. \tag{90}$$

D Appendix D: Oscillator amplitudes $A_\nu^{(nlj)}$

nlj	ε_{nlj}	$\nu=0$	$\nu=1$	$\nu=2$	$\nu=3$	$\nu=4$	$\nu=5$
$0s_{1/2}$	-17.661	0.997	-0.063	0.037	-0.022	0.004	-0.004
$0p_{3/2}$	-5.682	0.980	-0.154	0.110	-0.062	0.026	-0.015
$0p_{1/2}$	-0.806	0.940	-0.252	0.189	-0.110	0.061	-0.030
$0d_{5/2}$	4.596	0.870	-0.336	0.279	-0.192	0.115	-0.059
$1s_{1/2}$	3.985	0.075	0.771	-0.458	0.358	-0.228	0.106
$0d_{3/2}$	8.151	0.616	-0.487	0.445	-0.346	0.231	-0.115

Table 15: Woods-Saxon energies ε_{nlj} and oscillator amplitudes $A_\nu^{(nlj)}$ for proton single-particle states in ^{10}C, calculated using the WS parameters from Eqs. (66)-(68).

nlj	ε_{nlj}	$\nu=0$	$\nu=1$	$\nu=2$	$\nu=3$	$\nu=4$	$\nu=5$
$0s_{1/2}$	-19.868	0.997	-0.068	0.030	-0.021	0.003	-0.003
$0p_{3/2}$	-8.229	0.983	-0.146	0.094	-0.055	0.021	-0.012
$0p_{1/2}$	-3.977	0.960	-0.212	0.154	-0.086	0.044	-0.022
$0d_{5/2}$	2.071	0.898	-0.309	0.244	-0.164	0.094	-0.048
$1s_{1/2}$	1.775	0.076	0.799	-0.439	0.331	-0.208	0.095
$0d_{3/2}$	5.818	0.687	-0.465	0.409	-0.307	0.200	-0.099

Table 16: Woods-Saxon energies ε_{nlj} and oscillator amplitudes $A_\nu^{(nlj)}$ for neutron single-particle states in ^{12}Be, calculated using the WS parameters from Eqs. (66)-(68).

nlj	ε_{nlj}	$\nu=0$	$\nu=1$	$\nu=2$	$\nu=3$	$\nu=4$	$\nu=5$
$0s_{1/2}$	-24.512	0.999	-0.004	0.019	-0.015	-0.001	-0.003
$0p_{3/2}$	-11.768	0.996	-0.046	0.062	-0.033	0.007	-0.008
$0p_{1/2}$	-6.005	0.987	-0.104	0.111	-0.050	0.023	-0.014
$0d_{5/2}$	0.186	0.965	-0.168	0.165	-0.096	0.049	-0.028
$1s_{1/2}$	1.224	0.014	0.884	-0.340	0.270	-0.159	0.069
$0d_{3/2}$	6.429	0.766	-0.410	0.370	-0.266	0.173	-0.086

Table 17: Woods-Saxon energies ε_{nlj} and oscillator amplitudes $A_\nu^{(nlj)}$ for proton single-particle states in ^{12}C, calculated using the WS parameters from Eqs. (66)-(68).

nlj	ε_{nlj}	$\nu=0$	$\nu=1$	$\nu=2$	$\nu=3$	$\nu=4$	$\nu=5$
$0s_{1/2}$	-13.934	0.988	-0.137	0.059	-0.034	0.011	-0.006
$0p_{3/2}$	-3.307	0.942	-0.267	0.166	-0.103	0.052	-0.026
$0p_{1/2}$	-0.055	0.810	-0.427	0.311	-0.212	0.128	-0.061
$0d_{5/2}$	-0.064	0.953	-0.197	0.191	-0.110	0.061	-0.033
$1s_{1/2}$	-0.064	-0.003	0.882	-0.340	0.278	-0.158	0.070
$0d_{3/2}$	-0.053	0.964	-0.115	0.213	-0.082	0.064	-0.027

Table 18: Woods-Saxon energies ε_{nlj} and oscillator amplitudes $A_\nu^{(nlj)}$ for neutron single-particle states in ^{10}Be, calculated using Wang's parametrization (see subsection 3.2.1).

nlj	ε_{nlj}	$\nu=0$	$\nu=1$	$\nu=2$	$\nu=3$	$\nu=4$	$\nu=5$
$0s_{1/2}$	-16.159	0.995	-0.082	0.041	-0.024	0.005	-0.004
$0p_{3/2}$	-4.551	0.972	-0.183	0.122	-0.071	0.032	-0.017
$0p_{1/2}$	-0.045	0.925	-0.281	0.207	-0.125	0.070	-0.034
$0d_{5/2}$	-0.085	0.971	-0.137	0.166	-0.087	0.046	-0.027
$1s_{1/2}$	-0.066	-0.040	0.922	-0.265	0.244	-0.128	0.056
$0d_{3/2}$	-0.044	0.474	-0.518	0.495	-0.406	0.278	-0.138

Table 19: Woods-Saxon energies ε_{nlj} and oscillator amplitudes $A_\nu^{(nlj)}$ for proton single-particle states in ^{10}C, calculated using Wang's parametrization (see subsection 3.2.1).

nlj	ε_{nlj}	$\nu=0$	$\nu=1$	$\nu=2$	$\nu=3$	$\nu=4$	$\nu=5$
$0s_{1/2}$	-12.429	0.982	-0.172	0.064	-0.039	0.013	-0.007
$0p_{3/2}$	-2.733	0.929	-0.298	0.176	-0.112	0.058	-0.028
$0p_{1/2}$	-0.056	0.877	-0.364	0.249	-0.163	0.093	-0.045
$0d_{5/2}$	-0.052	0.948	-0.217	0.188	-0.115	0.061	-0.033
$1s_{1/2}$	-0.051	0.022	0.877	-0.352	0.274	-0.161	0.070
$0d_{3/2}$	-0.066	0.498	-0.522	0.487	-0.393	0.266	-0.131

Table 20: Woods-Saxon energies ε_{nlj} and oscillator amplitudes $A_\nu^{(nlj)}$ for neutron single-particle states in ^{12}Be, calculated using Wang's parametrization (see subsection 3.2.1).

nlj	ε_{nlj}	$\nu=0$	$\nu=1$	$\nu=2$	$\nu=3$	$\nu=4$	$\nu=5$
$0s_{1/2}$	-20.843	0.999	-0.040	0.024	-0.019	0.001	-0.003
$0p_{3/2}$	-8.776	0.991	-0.100	0.078	-0.045	0.014	-0.010
$0p_{1/2}$	-3.715	0.973	-0.167	0.136	-0.071	0.035	-0.019
$0d_{5/2}$	-0.043	0.968	-0.160	0.161	-0.093	0.047	-0.027
$1s_{1/2}$	-0.065	0.049	0.834	-0.403	0.309	-0.191	0.086
$0d_{3/2}$	-0.058	0.706	-0.448	0.402	-0.300	0.197	-0.098

Table 21: Woods-Saxon energies ε_{nlj} and oscillator amplitudes $A_\nu^{(nlj)}$ for proton single-particle states in ^{12}C, calculated using Wang's parametrization (see subsection 3.2.1).

nlj	ε_{nlj}	$\nu=0$	$\nu=1$	$\nu=2$	$\nu=3$	$\nu=4$	$\nu=5$
$0s_{1/2}$	-24.718	0.986	-0.165	-0.013	-0.010	0.006	0.002
$0p_{3/2}$	-17.203	0.988	-0.150	-0.005	-0.025	0.006	0.002
$0p_{1/2}$	-15.566	0.993	-0.117	0.004	-0.028	0.004	0.001
$0d_{5/2}$	-9.180	0.988	-0.148	0.027	-0.046	0.010	-0.002
$1s_{1/2}$	-6.641	0.157	0.952	-0.235	0.080	-0.076	0.022
$0d_{3/2}$	-5.906	0.988	-0.130	0.064	-0.057	0.015	-0.009
$0f_{7/2}$	-1.039	0.972	-0.190	0.099	-0.090	0.033	-0.017
$1p_{3/2}$	-0.051	0.127	0.882	-0.360	0.215	-0.160	0.064
$0f_{5/2}$	-0.044	0.982	-0.097	0.133	-0.085	0.033	-0.024
$1p_{1/2}$	-0.053	0.069	0.904	-0.319	0.220	-0.155	0.058

Table 22: Woods-Saxon energies ε_{nlj} and oscillator amplitudes $A_\nu^{(nlj)}$ for neutron single-particle states in ^{48}Ca, calculated using Wang's parametrization (see subsection 3.2.1).

nlj	ε_{nlj}	$\nu=0$	$\nu=1$	$\nu=2$	$\nu=3$	$\nu=4$	$\nu=5$
$0s_{1/2}$	-33.426	0.995	-0.095	-0.042	-0.012	0.003	0.004
$0p_{3/2}$	-25.211	0.998	-0.038	-0.040	-0.025	-0.001	0.004
$0p_{1/2}$	-22.864	0.999	0.009	-0.025	-0.026	-0.005	0.001
$0d_{5/2}$	-16.228	0.999	0.013	-0.021	-0.035	-0.007	0.001
$1s_{1/2}$	-12.060	0.094	0.994	-0.013	-0.001	-0.046	-0.006
$0d_{3/2}$	-11.324	0.997	0.064	0.018	-0.031	-0.008	-0.005
$0f_{7/2}$	-6.745	0.998	0.042	0.016	-0.044	-0.008	-0.005
$1p_{3/2}$	-2.431	0.037	0.991	-0.073	0.072	-0.077	0.004
$0f_{5/2}$	0.943	0.993	0.035	0.097	-0.050	0.010	-0.018
$1p_{1/2}$	-0.018	-0.009	0.984	-0.094	0.120	-0.087	0.013

Table 23: Woods-Saxon energies ε_{nlj} and oscillator amplitudes $A_\nu^{(nlj)}$ for proton single-particle states in ^{48}Ti, calculated using the WS parameters from Eqs. (66)-(68).

nlj	ε_{nlj}	$\nu=0$	$\nu=1$	$\nu=2$	$\nu=3$	$\nu=4$	$\nu=5$
$0s_{1/2}$	-24.595	0.989	-0.147	-0.028	-0.010	0.005	0.003
$0p_{3/2}$	-16.980	0.993	-0.111	-0.025	-0.024	0.003	0.004
$0p_{1/2}$	-14.929	0.997	-0.070	-0.013	-0.027	-0.001	0.001
$0d_{5/2}$	-8.690	0.996	-0.084	-0.001	-0.040	0.002	0.001
$1s_{1/2}$	-5.238	0.142	0.975	-0.154	0.038	-0.062	0.011
$0d_{3/2}$	-4.510	0.997	-0.051	0.037	-0.045	0.004	-0.007
$0f_{7/2}$	-0.054	0.992	-0.091	0.051	-0.066	0.012	-0.009
$1p_{3/2}$	-0.060	0.063	0.975	-0.158	0.103	-0.098	0.019
$0f_{5/2}$	-0.026	0.993	0.061	0.092	-0.043	0.006	-0.017
$1p_{1/2}$	-0.044	-0.009	0.985	-0.093	0.120	-0.087	0.012

Table 24: Woods-Saxon energies ε_{nlj} and oscillator amplitudes $A_\nu^{(nlj)}$ for proton single-particle states in ^{48}Ti, calculated using Wang's parametrization (see subsection 3.2.1).

E Appendix E: Talmi-Moshinsky transformation for Woods-Saxon wavefunctions in HO basis

Defining the two-body WS wavefunction as we did in Equation (75), we can expand the Talmi-Moshinsky transformation for double-beta decay as follows

$$
\begin{aligned}
&{}_{\rm WS}\langle n_1' l_1' j_1' p, n_2' l_2' j_2' p; J|O_\alpha|n_1 l_1 j_1 n, n_2 l_2 j_2 n; J\rangle_{\rm WS} = \\
&= \sum_{\nu_1\nu_2\nu_1'\nu_2'} A'_{\nu_1'}{}^{(n_1' l_1' j_1')} A'_{\nu_2'}{}^{(n_2' l_2' j_2')} A^{(n_1 l_1 j_1)}_{\nu_1} A^{(n_2 l_2 j_2)}_{\nu_2} {}_{\rm HO}\langle \nu_1' l_1' j_1' p, \nu_2' l_2' j_2' p; J|O_\alpha|\nu_1 l_1 j_1 n, \nu_2 l_2 j_2 n; J\rangle_{\rm HO} = \\
&= \sum_{S,S',\lambda,\lambda'} \sqrt{\hat{j}_1'\hat{j}_2'\hat{S}'\hat{\lambda}'}\sqrt{\hat{j}_1\hat{j}_2\hat{S}\hat{\lambda}} \begin{Bmatrix} l_1' & \frac{1}{2} & j_1 \\ l_2' & \frac{1}{2} & j_2 \\ \lambda' & S' & J \end{Bmatrix} \begin{Bmatrix} l_1 & \frac{1}{2} & j_1 \\ l_2 & \frac{1}{2} & j_2 \\ \lambda & S & J \end{Bmatrix} \langle l_1' l_2' \lambda', S', J|S_\alpha|l_1 l_2 \lambda, S, J\rangle \\
&\quad \sum_{\nu_1\nu_2\nu_1'\nu_2'} A'_{\nu_1'}{}^{(n_1' l_1' j_1')} A'_{\nu_2'}{}^{(n_2' l_2' j_2')} A^{(n_1 l_1 j_1)}_{\nu_1} A^{(n_2 l_2 j_2)}_{\nu_2} \langle \nu_1' l_1', \nu_2' l_2'|H_\alpha(r)\tilde{H}_\alpha(R)|\nu_1 l_1, \nu_2 l_2\rangle = \\
&= \sum_{S,S',\lambda,\lambda'} \sqrt{\hat{j}_1'\hat{j}_2'\hat{S}'\hat{\lambda}'}\sqrt{\hat{j}_1\hat{j}_2\hat{S}\hat{\lambda}} \begin{Bmatrix} l_1' & \frac{1}{2} & j_1 \\ l_2' & \frac{1}{2} & j_2 \\ \lambda' & S' & J \end{Bmatrix} \begin{Bmatrix} l_1 & \frac{1}{2} & j_1 \\ l_2 & \frac{1}{2} & j_2 \\ \lambda & S & J \end{Bmatrix} \\
&\quad \sum_{\nu,\nu',l,l',N,N',L,L'} \langle l' L' \lambda', S', J|S_\alpha|l L \lambda, S, J\rangle \sum_{\nu_1\nu_2\nu_1'\nu_2'} A'_{\nu_1'}{}^{(n_1' l_1' j_1')} A'_{\nu_2'}{}^{(n_2' l_2' j_2')} A^{(n_1 l_1 j_1)}_{\nu_1} A^{(n_2 l_2 j_2)}_{\nu_2} \\
&\quad \langle \nu_1' l_1', \nu_2' l_2'|\nu' l', N' L'\rangle_{\lambda'} \langle \nu_1 l_1, \nu_2 l_2|\nu l, N L\rangle_{\lambda} \langle \nu' l', N' L'|H_\alpha(r)\tilde{H}_\alpha(R)|\nu l, N L\rangle \\
&= \sum_{S,S',\lambda,\lambda'} \sqrt{\hat{j}_1'\hat{j}_2'\hat{S}'\hat{\lambda}'}\sqrt{\hat{j}_1\hat{j}_2\hat{S}\hat{\lambda}} \begin{Bmatrix} l_1' & \frac{1}{2} & j_1 \\ l_2' & \frac{1}{2} & j_2 \\ \lambda' & S' & J \end{Bmatrix} \begin{Bmatrix} l_1 & \frac{1}{2} & j_1 \\ l_2 & \frac{1}{2} & j_2 \\ \lambda & S & J \end{Bmatrix} \\
&\quad \sum_{\nu,\nu',l,l',N,N',L,L'} \langle l' L' \lambda', S', J|S_\alpha|l L \lambda, S, J\rangle \sum_{\nu_1\nu_2\nu_1'\nu_2'} A'_{\nu_1'}{}^{(n_1' l_1' j_1')} A'_{\nu_2'}{}^{(n_2' l_2' j_2')} A^{(n_1 l_1 j_1)}_{\nu_1} A^{(n_2 l_2 j_2)}_{\nu_2} \\
&\quad \langle \nu_1' l_1', \nu_2' l_2'|\nu' l', N' L'\rangle_{\lambda'} \langle \nu_1 l_1, \nu_2 l_2|\nu l, N L\rangle_{\lambda} \langle \nu' l'|H_\alpha(r)|\nu l\rangle \langle N' L'|\tilde{H}_\alpha(R)|N L\rangle \\
&= \sum_{S,S',\lambda,\lambda'} \sqrt{\hat{j}_1'\hat{j}_2'\hat{S}'\hat{\lambda}'}\sqrt{\hat{j}_1\hat{j}_2\hat{S}\hat{\lambda}} \begin{Bmatrix} l_1' & \frac{1}{2} & j_1 \\ l_2' & \frac{1}{2} & j_2 \\ \lambda' & S' & J \end{Bmatrix} \begin{Bmatrix} l_1 & \frac{1}{2} & j_1 \\ l_2 & \frac{1}{2} & j_2 \\ \lambda & S & J \end{Bmatrix} \\
&\quad \sum_{\nu,\nu',l,l',N,N',L,L'} \langle l' L' \lambda', S', J|S_\alpha|l L \lambda, S, J\rangle \sum_{\nu_1\nu_2\nu_1'\nu_2'} A'_{\nu_1'}{}^{(n_1' l_1' j_1')} A'_{\nu_2'}{}^{(n_2' l_2' j_2')} A^{(n_1 l_1 j_1)}_{\nu_1} A^{(n_2 l_2 j_2)}_{\nu_2} \\
&\quad \langle \nu_1' l_1', \nu_2' l_2'|\nu' l', N' L'\rangle_{\lambda'} \langle \nu_1 l_1, \nu_2 l_2|\nu l, N L\rangle_{\lambda} \langle \nu' l'|H_\alpha(r)|\nu l\rangle \delta_{N,N'}\delta_{L,L'}.
\end{aligned}
$$

Since most of the times $\tilde{H}_\alpha(R) = 1$, in the last step of the development we have considered $\langle N' L'|\tilde{H}_\alpha(R)|N L\rangle = \delta_{N,N'}\delta_{L,L'}$.

References

[1] L. Cardani. Neutrinoless double beta decay overview. *SciPost Physics Proceedings*, 02 2019.

[2] C. Patrignani et al. Review of Particle Physics. *Chin. Phys. C*, 40(10):100001, 2016.

[3] Jonathan Engel and Javier Menéndez. Status and future of nuclear matrix elements for neutrinoless double-beta decay: a review. *Reports on Progress in Physics*, 80(4):046301, Mar 2017.

[4] J. Kotila and F. Iachello. Phase-space factors for double-β decay. *Phys. Rev. C*, 85:034316, Mar 2012.

[5] KATRIN Collaboration and KATRIN Collaboration. Katrin design report 2004. Technical report, Forschungszentrum, Karlsruhe, 2005. 51.54.01; LK 01.

[6] N. Aghanim, Y. Akrami, M. Ashdown, J. Aumont, C. Baccigalupi, M. Ballardini, A. J. Banday, R. B. Barreiro, N. Bartolo, and et al. Planck 2018 results. *Astronomy Astrophysics*, 641:A6, Sep 2020.

[7] M. Biassoni and O. Cremonesi. Search for neutrino-less double beta decay with thermal detectors. *Progress in Particle and Nuclear Physics*, 114:103803, 2020.

[8] Sacha Davidson, Enrico Nardi, and Yosef Nir. Leptogenesis. *Physics Reports*, 466(4):105 – 177, 2008.

[9] Vincenzo Cirigliano, Wouter Dekens, Emanuele Mereghetti, and André Walker-Loud. Neutrinoless double-β decay in effective field theory: The light-majorana neutrino-exchange mechanism. *Phys. Rev. C*, 97:065501, Jun 2018.

[10] A. Gando, Y. Gando, T. Hachiya, A. Hayashi, S. Hayashida, H. Ikeda, K. Inoue, K. Ishidoshiro, Y. Karino, M. Koga, S. Matsuda, T. Mitsui, K. Nakamura, S. Obara, T. Oura, H. Ozaki, I. Shimizu, Y. Shirahata, J. Shirai, A. Suzuki, T. Takai, K. Tamae, Y. Teraoka, K. Ueshima, H. Watanabe, A. Kozlov, Y. Takemoto, S. Yoshida, K. Fushimi, T. I. Banks, B. E. Berger, B. K. Fujikawa, T. O'Donnell, L. A. Winslow, Y. Efremenko, H. J. Karwowski, D. M. Markoff, W. Tornow, J. A. Detwiler, S. Enomoto, and M. P. Decowski. Search for majorana neutrinos near the inverted mass hierarchy region with kamland-zen. *Phys. Rev. Lett.*, 117:082503, Aug 2016.

[11] Maria Goeppert Mayer. On closed shells in nuclei. ii. *Phys. Rev.*, 75:1969–1970, Jun 1949.

[12] Otto Haxel, J. Hans D. Jensen, and Hans E. Suess. On the "magic numbers" in nuclear structure. *Phys. Rev.*, 75:1766–1766, Jun 1949.

[13] Etienne Caurier. Shell model and nuclear structure. *Progress in Particle and Nuclear Physics*, 59(1):226 – 242, 2007. International Workshop on Nuclear Physics 28th Course.

[14] Alfredo Poves and Frederic Nowacki. *The nuclear shell model*, pages 70–101. Springer Berlin Heidelberg, Berlin, Heidelberg, 2001.

[15] E. Caurier, G. Martínez-Pinedo, F. Nowacki, A. Poves, and A. P. Zuker. The shell model as a unified view of nuclear structure. *Rev. Mod. Phys.*, 77:427–488, Jun 2005.

[16] Present status of shell model techniques.

[17] Main website of the shell model code ANTOINE. http://www.iphc.cnrs.fr/nutheo/code_antoine/menu.html.

[18] Masaru Doi, Tsuneyuki Kotani, and Eiichi Takasugi. Double Beta Decay and Majorana Neutrino. *Progress of Theoretical Physics Supplement*, 83:1–175, 03 1985.

[19] Mattias Blennow, Enrique Fernandez-Martinez, Jacobo Lopez-Pavon, and Javier Menéndez. Neutrinoless double beta decay in seesaw models. *Journal of High Energy Physics*, 2010(7), Jul 2010.

[20] Meng Wang, G. Audi, F. G. Kondev, W.J. Huang, S. Naimi, and Xing Xu. The AME2016 atomic mass evaluation (II). tables, graphs and references. *Chinese Physics C*, 41(3):030003, mar 2017.

[21] Website of the Atomic Mass Data Center. http://amdc.impcas.ac.cn/.

[22] Evaluated Nuclear Structure Data File of the National Nuclear Data Center. http://amdc.impcas.ac.cn/.

[23] Matthew Redshaw, Georg Bollen, Maxime Brodeur, Scott Bustabad, David L. Lincoln, Samuel J. Novario, Ryan Ringle, and Stefan Schwarz. Atomic mass and double-beta-decay Q value of Ca-48. *Phys. Rev. C*, 86:041306, 2012.

[24] M. Redshaw, E. Wingfield, J. McDaniel, and E.G. Myers. Mass and double-beta-decay Q value of Xe-136. *Phys. Rev. Lett.*, 98:053003, 2007.

[25] E. Caurier, F. Nowacki, and A. Poves. Shell Model description of the $\beta\beta$ decay of 136Xe. *Physics Letters B*, 711(1):62–64, May 2012.

[26] Fedor Šimkovic, Rastislav Dvornický, Du šan Štefánik, and Amand Faessler. Improved description of the $2\nu\beta\beta$-decay and a possibility to determine the effective axial-vector coupling constant. *Phys. Rev. C*, 97:034315, Mar 2018.

[27] X.B. Wang, A.C. Hayes, J. Carlson, G.X. Dong, E. Mereghetti, S. Pastore, and R.B. Wiringa. Comparison between variational monte carlo and shell model calculations of neutrinoless double beta decay matrix elements in light nuclei. *Physics Letters B*, 798:134974, Nov 2019.

[28] Jouni Suhonen. *From Nucleons to Nucleus: Concepts of Microscopic Nuclear Theory*. Theoretical and Mathematical Physics. Springer, Berlin, Germany, 2007.

[29] P. J Brussaard and (joint author.) Glaudemans, P. W. M. *Shell-model applications in nuclear spectroscopy*. Amsterdam ; New York : North-Holland Pub. Co. ; New York : sole distributors for the USA and Canada, Elsevier/North-Holland, 1977.

[30] F. Oberhettinger W. Magnus and R. P. Soni. Formulas and theorems for the special functions of mathematical physics. *ZAMM - Journal of Applied Mathematics and Mechanics / Zeitschrift für Angewandte Mathematik und Mechanik*, 47(8):554–554, 1967.

[31] J. Blomqvist and A. Molinari. Collective 0− vibrations in even spherical nuclei with tensor forces. *Nuclear Physics A*, 106(3):545 – 569, 1968.

[32] E. K. Warburton and B. A. Brown. Effective interactions for the 0p1s0d nuclear shell-model space. *Phys. Rev. C*, 46:923–944, Sep 1992.

[33] E.K. Warburton, B.A. Brown, and D.J. Millener. Large-basis shell-model treatment of a = 16. *Physics Letters B*, 293(1):7 – 12, 1992.

[34] D.H. Gloeckner and R.D. Lawson. Spurious center-of-mass motion. *Physics Letters B*, 53(4):313 – 318, 1974.

[35] Alessandro Lovato. Private communication.

[36] Kenneth M. Nollett and R. B. Wiringa. Asymptotic normalization coefficients from "ab initio" calculations. *Physical Review C*, 83(4), Apr 2011.

[37] I. Talmi. *Helv. Phys*, Acta 25:185, 1952.

[38] Marcos Moshinsky. Transformation brackets for harmonic oscillator functions. *Nuclear Physics*, 13(1):104 – 116, 1959.

[39] Amos de Shalit, Igal Talmi, and H S W Massey. *Nuclear shell theory*. Pure Appl. Phys. Academic Press, New York, NY, 1963.